Viscous flow past a cylinder close to a free surface: benchmarks with steady, periodic and metastable responses, solved by meshfree and mesh-based schemes

A. Colagrossi[a], G. Nikolov[b], D. Durante[a], S. Marrone[a], A. Souto-Iglesias[c,*]

[a] *CNR-INM, INstitute of Marine engineering, Via di Vallerano 139, 00128 Rome, Italy.*
[b] *BSHC Bulgarian Ship Hydr. Centre at Bulgarian Academy of Sciences, Varna, Bulgaria*
[c] *CEHINAV, DMFPA, ETSIN, Universidad Politécnica de Madrid (UPM), Madrid, Spain*

Abstract

The question of whether it is possible to set relevant, robust and reliable benchmarks for viscous free-surface flows with complex free-surface dynamics is investigated in this work. The proposed method for finding an answer to this question consists of selecting three conditions leading to increasing flow complexity and to simulate them using three well established solvers based on diverse numerical techniques. In the three conditions, a submerged horizontal cylinder in an uniform current perpendicular to its axis is considered, the Reynolds number is fixed to 180, and the analysis is limited to a 2D framework. While the unbounded solution for such flow is well established, adding a free surface and setting the submergence ratio and the Froude number in certain ranges, challenging free-surface dynamics takes place. In the specific conditions selected, phenomena of increasing complexity are identified and studied with: (i) δ^+-SPH, an enhanced version of the Smoothed Particle Hydrodynamic method, (ii) a single-phase Finite Volume scheme with a Level Set function for tracking the free-surface (LS-FVM), (iii) a two-phase Finite Volume with a Volume-of-Fluid algorithm to treat the gas/liquid interface (VOF-FVM). It is shown that the test-cases, even being geometrically simple, present intricate complexities, such as alternate metastable states in the wake, linked to the strong non-linearities induced by the interactions between the wake's vorticity and the free surface. It is also shown that the solvers considered are able to depict a consistent representation of these complex flows, useful as benchmarks for other solvers and methods. An additional research question, investigating whether the improvements of the δ^+ variant of the SPH method are necessary for simulating specific aspects of the flows treated in the paper, is also posed and discussed.

Keywords: Smoothed Particle Hydrodynamics, SPH, free-surface flows, viscous flow past a cylinder, breaking waves, Finite Volume Method, Level Set function, Volume of Fluid, Von Kármán vortex street, metastable states.

*Corresponding author:
Email address: antonio.souto@upm.es (A. Souto-Iglesias)

1. Introduction

Open channel flow problems are of a great relevance in hydraulic engineering. The main difficulties arising in the numerical simulation of such kind of flows lay on the non trivial aspect of the presence of a free surface, which must be correctly modelled, whereas further issues are related to a suitable choice of inlet and outlet boundary conditions. In order to achieve satisfying solutions in terms time and space accuracy, numerous approaches have been developed in the recent years spanning from mesh-based Finite Volume Methods (FVM), to Smooth Particle Hydrodynamics (SPH) and Diffused Vortex Hydrodynamics (DVH) meshless approaches.

As an example, a weakly-compressible SPH model was used for studying different hydraulic jump conditions in Federico et al. (2012). Conversely, in (Marrone et al., 2013) the unbounded viscous flow around a circular cylinder at low Reynolds number (10-1000) was studied in order to validate the δ-SPH scheme, and the methodology chosen to enforce the no-slip boundary conditions. Indeed, the flow past blunt bodies is one of the most used benchmarks for validating Navier-Stokes solvers.

In those works, a weakly-compressible flow model was used, and the inflow/outflow conditions were implemented in a way that prevented permanent reflections of acoustic signals inside the fluid domain. From (Marrone et al., 2013), it is possible also to see that there is a non-negligible scattering between different results available in literature for the unbounded viscous flow around a cylinder at the referred Reynolds numbers. This is mainly due to the wide span in time of the articles where the different reference solutions can be found.

To overcome this issue, in this work, a convergent solution obtained with the DVH vortex method, for which an in-house solver is available, is considered. The DVH technique has been extensively validated, providing reference solutions for 2D-flows past bodies of different shapes (see *e.g.* (Rossi et al., 2015, 2016; Durante et al., 2017)).

Benchmark test-cases for viscous flows in the presence of a free surface are rare in the literature. An straightforward way to get these can be by adding a free surface to the unbounded flow past a circular cylinder. The landscape of flows that turns up is extremely rich, the reason being that to the already complex cylinder wake instabilities, a non-linear unsteady free-surface flow is added.

A referential work for this problem is the one carried out by Reichl et al. (2005) using a commercial code (ANSYS Fluent) based on a Finite Volume Method combined with a Volume-of-Fluid algorithm to resolve the air-water interface

(in the following the acronym VOF-FVM will be used for this solver). They investigated the 2D flow around a cylinder close to a free-surface, fixing the Reynolds number to 180. The latter is defined as $\mathrm{Re} = Ud/\nu = 180$, where U is the free-stream velocity, d the cylinder diameter and ν the kinematic viscosity.

Indeed, for unbounded flow past a cylinder it is possible to get practically bi-dimensional conditions in such low Reynolds number regime, something that is generally not true when a free-surface is present. It is relevant to mention that even though this is the case, Reichl et al. (2005) were able to reproduce the main flow features analyzed through the experimental study of Sheridan et al. (1997), for which the Reynolds number was approximately 9000, suggesting that for viscous flows around a cylinder in the presence of a free-surface, actually Froude number ($\mathrm{Fr} = U/\sqrt{(gd)}$, g is the gravity) and submergence ratio (h/d, h is the cylinder depth) are as important as the Reynolds number in order to characterize the dynamics.

However, from the numerical point of view, low Reynolds number regimes have the advantage of allowing performing simulations without the use of sub-grid models, which would complicate the already complex flow. Moreover, the sub-grid models are known to present limitations when turbulence is injected through breaking wave phenomena, this being still nowadays an open-problem.

Summarizing, in this work the choices made by Reichl et al. (2005) of low-Reynolds regime and a bidimensional framework are also adopted, as, even with such simplified hypothesis, the problem remains extremely complicated to be numerically solved, raising open questions relative to spectra of forces time histories, breaking patterns, etc.

Motivated by this complexity, the main research question behind this paper is whether it is possible to set relevant, robust and reliable benchmarks for viscous free-surface flows with complex free-surface dynamics. Such benchmarks would then be offered to be used as reference for other solvers when modeling free-surface geometry, forces, vorticity generation and other relevant aspects of the flow.

The proposed method for finding the answer to this question consists of selecting three conditions leading to increasing flow complexity and to simulate them using three well established solvers based on diverse numerical techniques:

1. an enhanced version of the Smoothed Particle Hydrodynamic model (called δ^+-SPH) (for details see (Sun et al., 2017)).
2. a single-phase Finite Volume with a Level Set function for capturing/tracking the free-surface (LS-FVM) (for details see (Di Mascio

et al., 2008)).

3. a two-phase Finite Volume with a Volume-of-Fluid algorithm to treat the air/water interface (VOF-FVM) (for details see (Versteeg and Malalasekera, 1995; Hirt and Nichols, 1981)).

The SPH simulations have been performed using the code SPH-flow, a software developed within a collaborative consortium composed of Ecole Centrale de Nantes, NEXTFLOW Software company and CNR-INSEAN. Conversely, for the LS-FVM solver the CNR-INSEAN in-house code Xnavis (Di Mascio et al., 2007) has been used, while for the third one, similarly to (Reichl et al., 2005), the commercial code ANSYS Fluent has been chosen. While solvers based on other techniques such as the Particle Finite Element Method (Gimenez and González, 2015; Gimenez et al., 2017) have been able to successfully model complex free-surface flows, the sample chosen is considered representative enough for the problem in hand.

It has to be mentioned that one of the cases studied is characterized by the onset of a particularly challenging dynamics, i.e., the so-called alternate metastable states in the cylinder wake (Sheridan et al., 1995). The presence of these alternate states leads reflects on the time histories of the force coefficients through a low frequency harmonic. Motivated by this paper aiming to contribute to the Computers & Fluids "Special issue on Theoretical, numerical and computational advances of the SPH method for solving fluid problems", an additional research question is delineated, investigating whether the improvements of the δ^+ variant of the SPH method are necessary for simulating the onset and dynamics of such metastable states.

The research questions and method chosen lead to the paper contents being organized as follows:

- In section 2, the description of the physical problem, with its various parameters involved, is first described. In particular, it is discussed how the relevant dimensionless numbers have different effects depending on the solver adopted.

- Three test-cases of increasing complexities have been identified with a careful choice of the parameters. In section 3 the description of these different flows is given.

- Section 4 contains the overview of the computational models considered.

- The FVM and δ^+-SPH solvers are used for solving the unbounded case, in order to check the quality of the results in this simplified condition. Section 5 is dedicated to this preliminary test-case.
- In section 6 the results of the three solvers on the benchmark test-cases introduced in 2 section are compared.
- Finally, in section 7, it is justified that the shifting particle technique, embedded in the δ^+-SPH, is crucial for solving the third benchmark. Indeed, it shown that with δ-SPH it is not possible to accurately simulate this case.
- Conclusions are summarized to close the paper.

2. Description of the physical problem

A sketch of this problem is given in Figure 1. It consists of an open-channel flow with a circular cylinder inside the fluid domain, Ω, confined by:

1) a solid bottom $\partial\Omega_B$,

2) a free surface $\partial\Omega_F$

3) the cylinder surface $\partial\Omega_C$,

4) an inflow boundary $\partial\Omega_I$ on the left lateral side,

5) an outflow boundary $\partial\Omega_O$ on the right lateral side.

Since the vortex dynamics shed by the cylinder is the only one investigated in this work, on the cylinder surface $\partial\Omega_C$ a no-slip condition is considered while a simple free-slip condition is enforced on the bottom surface $\partial\Omega_B$.

In the initial time instant, the fluid is considered at rest, and $\partial\Omega_F$ is flat. In such a condition, the initial total water height of the channel is $\hat{H}$. The top part of the cylinder is at a distance H from the bottom, while h is the cylinder depth, defined as the gap distance between the cylinder top and the undisturbed free surface (*i.e.* $\hat{H} = H + h$).

The $x-$coordinates of $\partial\Omega_I$ and $\partial\Omega_O$ are respectively x_1 and x_2. In the inflow boundary, $\partial\Omega_I$, a vertical uniform velocity U and a hydrostatic pressure profile are imposed, and the water height is fixed to $\hat{H}$. In the outflow boundary, $\partial\Omega_O$, a zero-gradient boundary condition for the velocity field and a hydrostatic pressure profile are imposed. The water height is free to change following the

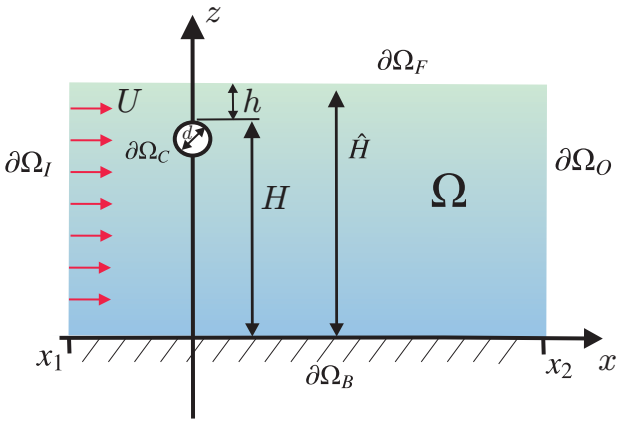

Figure 1: Case setup notation (borrowed from Reichl et al. (2005)) and system of reference.

flow dynamics, implying that the hydrostatic pressure profile imposed on $\partial\Omega_O$ depends on the water height on this boundary. In section 5, it is justified that the outflow conditions on $\partial\Omega_O$ must be enriched to prevent wave reflections from the downstream boundary.

The four main dimensionless numbers governing the problem are:

i) The Reynolds number $\mathrm{Re} = Ud/\nu$,

ii) The Froude number $\mathrm{Fr} = U/\sqrt{gd}$,

iii) The cylinder submergence ratio h/d,

iv) The Bond number $\mathrm{Bo} = \rho g d^2/\sigma$

where σ is the surface tension, and the other variables have been already introduced.

Surface tension can play a relevant role if a breaking wave is formed behind the cylinder (see *e.g.* (Landrini et al., 2012)). However, for the sake of simplicity, similarly to (Reichl et al., 2005), in this work the Bo number is assumed sufficiently high to neglect surface tension effects on the studied flows.

The Froude number governs the free-surface dynamics while the cylinder submergence governs the interaction between the body wake and the free-surface dynamics. Reichl et al. (2005) set the Reynolds number Re to 180, the Froude number ranges, $0.15 - 0.60$, and the cylinder submergence ratio, h/d, to vary from

0.1 up to 2.5. The range of analyzed configurations for Re = 180, regarding Fr and h/d, was extended by Bouscasse et al. (2017) using the $\delta-$SPH model.

In spite of the geometrical simplicity of the problem considered, some complexities need to be carefully treated:

1) the effect of the bottom $\partial\Omega_B$ on the flow,

2) the use of numerical damping zones in the proximity of in/out-flow boundaries,

3) the use of a time-ramp for the flow rate in the initial part of the simulation,

4) the necessity of a suitable spatial resolution on the far far-field region,

5) difficulties in obtaining numerical solutions totally independent by the spatial resolution,

6) two-phase versus single-phase model,

7) the lack of experimental data for validation

In the following subsections, these aspects are documented, discussing the strategies adopted by the selected computational models to deal with them.

2.1. The effect of the bottom on the flow

The radiation conditions can be easily enforced when using mesh-based models. Indeed, using a stretching of the mesh, the fluid domain boundaries $\partial\Omega_B$, $\partial\Omega_I$, $\partial\Omega_O$ can be set far enough in order not to influence the near-field of the body.

This is not the case when using particle methods like SPH, for which techniques to modify the particle size, such as the variable smoothing length (see *e.g.* (Hernquist and Katz, 1989; Bonet and Rodriguez-Paz, 2005)), are not trivial to be extended to the context of open-channel flows (to the authors knowledge, there are no works in the literature about this topic). Even the use of variable resolution techniques such as the one presented by Vacondio et al. (2013) or the more recent one published by Chiron et al. (2018b) (and used in (Sun et al., 2018)) cannot be easily adapted in the present work. Indeed, to our experience, the errors linked to the interaction of particle of different sizes or the ones related to the interpolation of the fields in the different sub-domains can alter the equilibrium of the channel flow, leading to a non-physical drift of the long-time solution (see (Colagrossi et al., 2017b)). For the above reasons, in the present work uniform

particle distribution is adopted, as further commented in section 3, leaving the topic of the SPH multi-resolution approach for open-channel flow simulations to future studies.

Because of the SPH difficulties in handling large fluid domains, in our problem $\partial\Omega_B$ can affect not only the near-field of the body but also the far field, as the free-surface motion can be indeed influenced by the treatment of the bottom boundary.

Another challenge for the SPH model related to the bottom is linked to the weakly compressibility assumption of the fluid model. Indeed, in order to remain in this condition, the artificial speed of sound, c_0 needs to be set large enough so that the hydrostatic pressure on the bottom cannot induce density variations larger than 1%. Following Antuono et al. (2011), this above constraint implies:

$$c_0 = 10\sqrt{g\hat{H}}. \tag{1}$$

Therefore, large $\hat{H}$ leads not only to a large number of particles but also to small time steps, considerably increasing the CPU costs.

Following the recommendations in (Bouscasse et al., 2017), for the three cases studied $\hat{H}/d$ is fixed to 16. Evaluating the Froude number $\mathrm{Fr}_{\hat{H}} = U/\sqrt{g\hat{H}}$, it results that for all the cases studied in this work, $\mathrm{Fr}_{\hat{H}}$ is always below 0.25. This threshold guarantees a limited effect of $\partial\Omega_B$ on the solutions.

If bottom effects are to be completely avoided, the problem we are presenting can be more efficiently solved by the coupling of SPH with a mesh-based solver, as demonstrated by Chiron et al. (2018a). However, in the present work, for the sake of a better understanding of the influence of the matters involved, the problem is studied with a monolithic SPH solver.

2.2. Use of numerical damping zones in the proximity of inflow/outflow boundaries

In the open-channel flow problem studied here, gravity waves can be generated by the flow around the cylinder and they can travel in both upstream and downstream directions. When these waves reach the inflow/outflow boundaries, they can introduce undesirable changes in the properties of the flow, if not properly transported outside of the domain. In addition to the gravity waves, the "equilibrium" of the flow is also influenced when the wake of the body reaches the outflow; for example, when a big vortex structure crosses the outflow, the water height changes and a gravity wave can be generated and propagated upstream. Hence, the choice of the inflow, x_1, and outflow, x_2, coordinates can affect the

solution, especially the long-time evolution when waves or vortices may reach those boundaries. Regardless of how large the fluid domain is, there always exists a time when the simulation will be affected by the above conditions.

Again, for the FVM solvers, the mesh stretching in the horizontal directions can help in dissipating both the gravity waves and the wake. Usually, the mesh stretching is not sufficient to avoid spurious waves reflections, and a numerical sponge (damping) region in the proximity of $\partial\Omega_I$ and $\partial\Omega_O$ must be implemented for stabilizing the flow. In the present work, this damping effect is achieved with a linear increase of the viscosity , starting from a given distance, $8d$, from inflow/outflow boundaries. The viscosity is increased by a factor of 10 when reaching $\partial\Omega_I$ and $\partial\Omega_O$. Moreover, also a damping term of the same intensity on the vertical flow acceleration has been added, following the technique by Molteni et al. (2013).

The implementation of these sponge regions has been tested on the three solvers imposing a sinusoidal vertical motion on the cylinder and checking that the radiated waves were dissipated without generating any wave reflections. For these tests, the free-stream current has been switched off.

The positions of $\partial\Omega_I$ and $\partial\Omega_O$ have been set equal to $x_1/d = -15$, and $x_2/d = 30$, for all the simulations .

2.3. Use of a time-ramp for the flow rate in the initial part of the simulation

For all the simulations, the following time-law is used for the free-stream speed:

$$U(t) = U \begin{cases} \left[3\left(\dfrac{t}{t_0}\right)^2 - 2\left(\dfrac{t}{t_0}\right)^3\right], & t < t_0; \\ 1, & t \geq t_0, \end{cases} \tag{2}$$

with $t_0\, U/d = 5$, d/U being the residence time, used to make time non-dimensional in what follows.

For consistency, an acceleration dU/dt has to be added in the momentum equation in order to accelerate all the fluid in Ω until the inflow steady condition is reached.

The use of the time-ramp for the flow rate has a double advantage: from the numerical point of view, it avoids a sudden start and subsequent generation of a pressure shock wave when using a weakly compressible SPH model. Also, its corresponding reflections on $\partial\Omega$ are prevented. The second advantage is that we can compare the solution of the three solvers also on the transient stage, and not only if steady state or periodic regimes are established.

2.4. *Necessity of a suitable spatial resolution in the far far-field region*

As shown in (Bouscasse et al., 2017), for a high enough Froude number, the von Kármán shedding mechanism is inhibited by the formation of a jet-flow over the cylinder, which induces long recirculation zones behind it. The recirculation areas need to be accurately resolved, thus limiting the possibility to reduce much the spatial resolution in the far field. Therefore, also for the LS-FVM and VOF-FVM solver, the mesh has to be designed in a suitable way in order to avoid unphysical drift of the solution (see section 4). This matter is paid however no attention by Reichl et al. (2005).

2.5. *Difficulties in obtaining numerical solutions totally independent of the spatial resolution*

The generation of gravity waves and the presence of the cylinder wake generally imply a strong unsteadiness of the flow in the initial transient stage. It is shown in this work that, in order to reach stable and regular flow evolutions, rather long time intervals for the simulations are needed. From the above considerations regarding the effects of the boundaries $\partial\Omega_B$, $\partial\Omega_I$ and $\partial\Omega_O$, we have already pointed out that also a rather large domain Ω is required. As a consequence of the large space-time domains and of a suitable spatial resolution up to the far far-field region, it results that even in a 2D framework, the CPU costs can be demanding.

The main consequence of this, added, on one side, to the highly non-linear interactions between the vortex wake and the free surface, and, on the other side, to the non-existence of a minimum theoretical length scale in interfacial flows, is the difficulty in getting solutions totally independent of the spatial resolution. As remarked in section 5, this is possible for the unbounded problem (removing $\partial\Omega_S$). Therefore, we preliminary tested the solvers on this problem, ensuring that the codes are able to give solutions close enough to a convergent one, obtained through a Particle Vortex Method (errors less than 4% on the forces, see section 5). Once this objective is achieved, the viscous free-surface benchmarks are tackled (see section 6).

2.6. *Two-phase versus single-phase model*

When breaking events occur, entrapment of air bubbles can take place and resulting buoyancy effects alter the near wake flow. In order to investigate such effect, the two FVM solvers have different models. The LS-FVM is based on a single-phase approach, as it is the δ^+-SPH. Conversely, the VOF-FVM adopts a two-phase model. It is shown in this paper that for the three test cases selected,

the effects of the air entrainment imply negligible effects on the flow dynamics and on the global loads acting on the cylinder (see section 6).

2.7. Lack of experimental data for validation

As explained, a 2D framework is used and the Reynolds number is set to a low value (180), in order to limit the computational needs and the local complexity of the flow. At the same time, in order to generate large deformations of the free surface, the Froude number ranges between 0.3 and 1.0. Combining these two dimensionless numbers and considering as a liquid the water, it results that the diameter of the cylinder d is of the order of a few millimeters. As a consequence, the Bond number is very low, of order 0.1, and the surface tension would dominate the free-surface dynamics. Besides, the small cylinder dimension would imply a lot of complexities from a point of view of the experimental facility. Working with an oil, a cylinder of few centimetres could be used. However, the use of an oil instead of simple water would lead again to complex issues in the experimental setup. For these reasons, it is not possible to find experimental data available for the benchmark test-cases proposed in this work.

However, since the Froude number is the one that dominates the flow, it is possible to see that the flow features observed in present research are in fair agreement with the experimental observations of Sheridan et al. (1997), where the Reynolds number is about 9000, while the highest Froude number is 0.72. Bond number is actually of order 10 in those experiments, implying that the surface tension may still play a role, and its effects not completely negligible. Moreover, neither Sheridan et al. (1995) nor Sheridan et al. (1997) present time histories of the forces, which could at least allow to try and set a time reference to establish corresponding times in the experiments and simulations. They only mentioned that the Strouhal number of the main shedding is of the order of 0.1 and the subharmonic's 0.001 in their experiments, leaving the matter open to further investigation. We hope our detailed description in the present paper can contribute to such aim.

3. Description of the proposed benchmark test-cases

A description of the proposed benchmarks of the flow past a submerged cylinder close to the free surface is provided in this section.

The distance between the cylinder and the free surface is set equal to $h/d = 0.4$ in order to get strong enough interaction between the cylinder wake and the free surface. The Reynolds number, as stressed above, is set equal to 180. Three

different Froude numbers, 0.3, 0.55 and 1.00, are chosen in order for different flow regimes, corresponding to an increasing level of interaction, to occur.

Lyapunov exponent fields are shown in Figures 2-4 to highlight the coherent structures for the three conditions chosen (the interested reader is referred to work by Sun et al. (2016)). The δ^+-SPH numerical scheme is used for this purpose, considering its Lagrangian nature being suitable to directly monitor the time evolution of this quantity.

Benchmark I (Fr=0.3, h/d=0.4, Re=180): Von Kármán street below a free surface.. The regime Fr = 0.30 is sketched in Figure 2 and shows a weak interaction with the free surface, which remains rather flat downstream of the body.

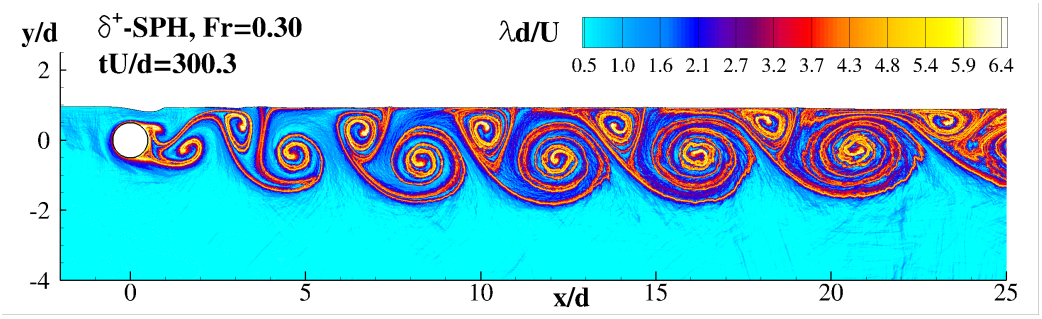

Figure 2: Case Fr = 0.3. The Lyapunov exponent is shown in order to highlight the vortical structures in the flow field. See supplementary material movie N.1a at http://canal.etsin.upm.es/papers/colagrossietalcaf2018/

The unbounded case periodic vortex shedding mechanism is still preserved, even though the presence of the free surface confines and deforms the shed dipoles similarly to a flat free-slip boundary. The little depression of the free surface, visible immediately after the cylinder, is due to the expected reduction of the pressure past the body. This case may be considered as the easiest to reproduce, the weak interaction making it very similar to an unbounded flow. The final time for the simulation has been set equal to $t_{end}U/d = 300$ in order to have enough oscillation periods in the periodic regime to properly define the mean value, amplitude and Strouhal number of the force coefficients.

Benchmark II (Fr=1.0, h/d=0.4, Re=180): spilling-jet flow regime.. Increasing the Froude number to Fr = 1.0, the flow is characterized by an intense spilling-jet flow over the cylinder, which inhibits the shedding mechanism, and creates a big

recirculation area, clearly visible in Figure 3. The free surface is characterized by a spilling breaking regime which leads to a stable flow condition. This is not the case during the initial transient regime where plunging breaking waves develop, causing a strong interaction with the cylinder wake. When the transient condition extinguishes, the recirculation region downstream of the cylinder and underneath the free surface extends to about $18d$, and needs to be accurately resolved in order to be correctly captured. The free surface ahead the cylinder shows an evident hump which affects the lift force value, whereas a fair characterization of the recirculation area allows a correct evaluation of the drag force. The final time of the previous test case is used $t_{end}U/d = 300$, long enough to achieve quasi steady state.

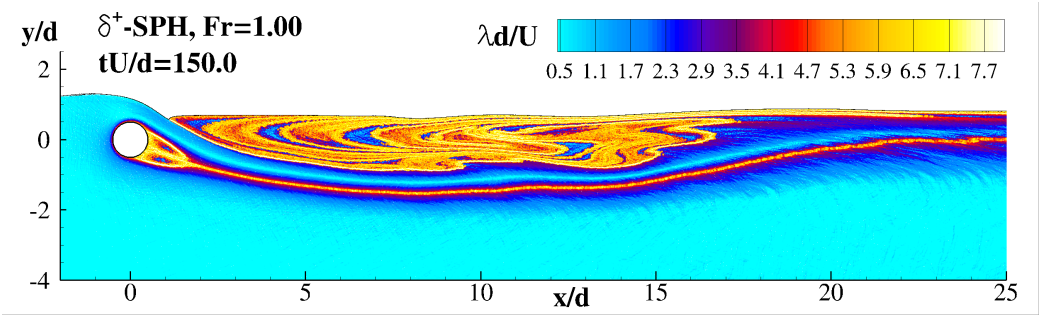

Figure 3: Case Fr = 1.0. The Lyapunov exponent is shown in order to highlight the vortical structures in the flow field. See supplementary material movie N.2a

Benchmark III (Fr=0.55, h/d=0.4, Re=180): the metastable flow condition.. Finally, the most complex case is the one corresponding Fr = 0.55, for which the flow changes with a continuous alternation between the two behaviors of the previous test-cases. Indeed, the spilling jet is still present but is weaker and in unstable equilibrium with the vortex shedding. The resulting flow is characterized by a low frequency switch between an intense vortex shedding (shown in the top plot of Figure 4) with an important free-surface deformation and a weak spilling jet (shown in the bottom plot of Figure 4), where the shedding mechanism is almost inhibited. The metastable flow induces a low frequency harmonic on the global loads. In order to capture enough periods of these low-frequency modes, the final time for the simulations has been set equal to $t_{end}U/d = 600$.

This peculiar phenomenon was described experimentally by Sheridan et al. (1995) (even though at different Reynolds numbers) and called “metastable”

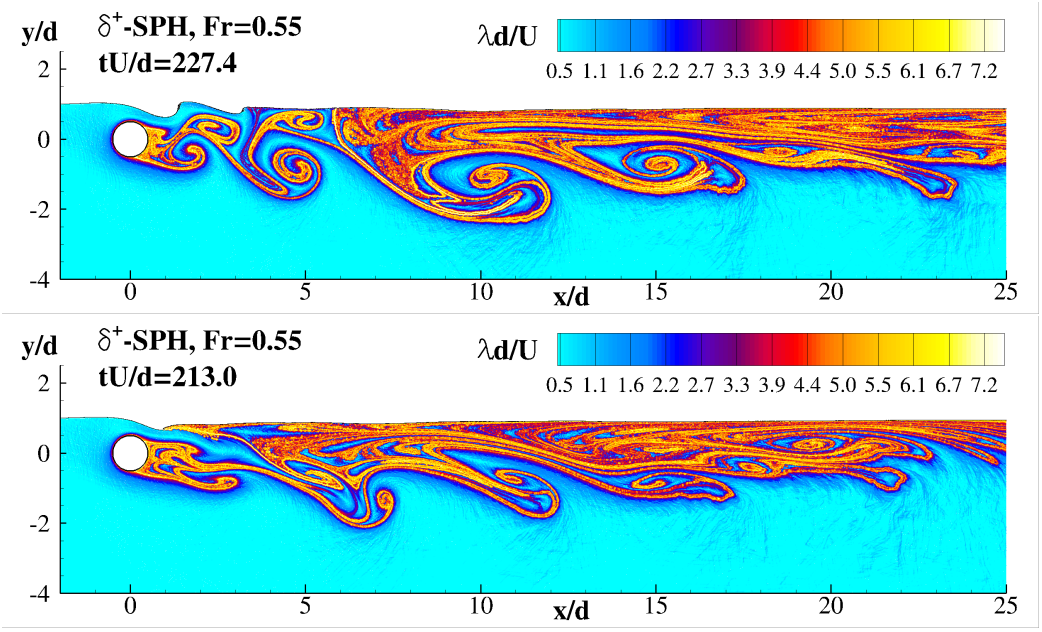

Figure 4: Case Fr = 0.55. Metastable regime: periodic vortex shedding (top), spilling jet flow (bottom). The Lyapunov exponent is shown in order to highlight the vortical structures in the flow field. See supplementary material movie N.3a

regime. In (Reichl et al., 2003), a metastable condition was found in numerical simulations with Re = 180 using a VOF-FVM solver. For the accurate reproduction of this test-case, a fine grid resolution in space and in time is required. In section 6, it will be shown that the metastable regime can also be captured by the LS-FVM and by the δ^+-SPH models. Conversely, the widely used δ-SPH model (Antuono et al., 2012) is not able to resolve this flow condition, and at Fr = 0.55 the numerical solution comes back to a pure spilling-jet flow, as will be discussed in section 7.

4. Summary of computational models adopted

4.1. SPH-flow code: single-phase δ^+-SPH model

The δ^+-SPH scheme, introduced by Sun et al. (2017), has been selected as the meshfree solver to deal with the benchmark proposed section 3. δ^+-SPH is an enhanced version of the weakly–compressible Smoothed Particle Hydrodynamic model for the solution of the Navier-Stokes equations. It is based on the δ-SPH

model (Antuono et al., 2012), where a diffusive term is added in the continuity equation to regularize the pressure/density field. In δ^+-SPH, a particle shifting technique is used to improve the regularity of the particle space distribution. In particular, the shifting technique proposed by Lind et al. (2012) is recast for the weakly-compressible formulations. Thanks to the small time steps, the magnitude of the particle shifting remains relatively small (in comparison with the incompressible SPH) resulting in quasi-lagrangian scheme (see also Oger et al. (2016); Khayyer et al. (2017). An algorithm for particle shifting at the free surface is also used, which however does not alter the actual free surface position (more details can be found in Sun et al. (2017)). Sun et al. (2017) demonstrated that with this SPH model it is possible to accurately solve the viscous flow past bodies of various shapes. It is therefore an appropriate candidate for the three proposed benchmarks of this work.

The fluid domain Ω is assumed to be discretized with N fluid particles which, for the sake of simplicity, are assumed to approximately have the same size, Δr, that represents the mean inter-particle distance. The resolution adopted in this work is $d/\Delta r = 100$. In the next section, it is shown how, through this resolution, is possible to get a very good agreement with the reference solution provided by the Diffused Vortex Hydrodynamics (DVH) method (see section 5). As explained by Sun et al. (2017), the pressure and viscous forces acting on a generic particle are evaluated by a Wendland C2 kernel through the interaction with its roughly 50 neighbor particles.

Since low Reynolds number flows are addressed in the present work no turbulence modeling is introduced in the scheme. Viscous stresses are modelled through the classic formula by Monaghan and Gingold (1983), whose derivation has been also recently discussed in Colagrossi et al. (2017a).

In order to enforce the boundary conditions on the body surface, a ghost-fluid technique is used. Various mirroring techniques can be adopted to enforce the required boundary conditions (i.e. free-slip on the bottom and no-slip on the cylinder). The details of the mirroring procedures adopted in this work can be found in (Bouscasse et al., 2013). The implementation of open boundary conditions is not trivial in SPH because of the Lagrangian nature of the method, with just few successful references in literature (Khorasanizade and Sousa, 2016; Federico et al., 2012; Lastiwka et al., 2008). These boundary conditions have been implemented in the present research using the technique described by Federico et al. (2012).

The δ^+-SPH model is embedded (together with other SPH models) in the software "SPH-flow", developed within a French-Italian collaborative consortium

(composed by Ecole Centrale de Nantes, NEXTFLOW Software company and CNR-INSEAN). Although this software also allows to use an Adaptive-Particle-Refinement technique, as explained in section 1, we have preferred to use a homogeneous particle distribution and leave the use of more complex algorithms for the future, as they are not sufficiently validated for open channel flows. This choice implies a large number of particles: the size of the domain Ω is about $45d \times 16d$ which leads $N \simeq 7$ millions.

Regarding the time integration, a 4th order Runge-Kutta scheme is adopted with the time step driven by the artificial speed of sound c_0. Following (Sun et al., 2017), the relation below holds:

$$\Delta t \;=\; 3\,\frac{\Delta r}{c_0}, \quad \Rightarrow \quad \Delta t\,\frac{U}{d} \;=\; 0.3\left(\frac{\Delta r}{d}\right)\mathrm{Fr}_{\hat{H}} \;=\; 7.5\,10^{-4}. \tag{3}$$

The time iterations are therefore about 800,000 for the longest simulation ($t_{end}U/d = 600$).

Thanks to the high scalability of the SPH-flow code, the simulations can be run on a small cluster in few days (see (Oger et al., 2016)).

Apart from the works already referred (Marrone et al., 2013; Federico et al., 2012; Bouscasse et al., 2017), SPH has been recently used to compute forces on cylinders by authors such as Aristodemo et al. (2017), who compared experiments and SPH results regarding the forces induced on a cylinder by a solitary wave, finding fair agreement between them.

4.2. Xnavis code: single-phase Finite Volume Method with Level-Set function (LS-FVM)

The Xnavis code is a general-purpose, second order, finite volume, multi-block solver, developed at CNR-INSEAN. The computation of the convective fluxes is achieved by several numerical schemes; for the present work a classical fourth order centered scheme has been chosen (for more details see Di Mascio et al. (2009)).

Viscous fluxes are discretized by means of the classical finite volume second order formulation. The free-surface effects are taken into account through a fully non-linear level-set single phase approach (Di Mascio et al., 2009; Broglia and Durante, 2017).

In order to have a fully implicit scheme and to obtain a divergence free velocity field, a dual (or pseudo) time-derivative is introduced in the discrete system of equations, and the solution is iterated up to a steady state in the pseudo time.

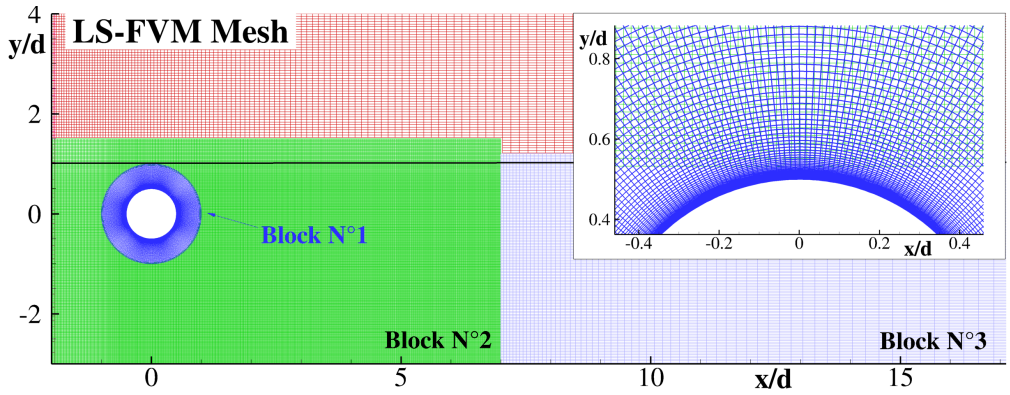

Figure 5: Sketch of the mesh used with the LS-FVM solver. The total number of computational cells is about 187,000. The horizontal line represents the undisturbed free surface. An enlarge view close to the cylinder surface is reported in the right box.

The full multi-grid approach and the implicit approximate factorization technique with local time stepping are used to speed up convergence of the internal iteration. The numerical mesh employed is based on a Chimera grid technique. In this approach, the overlapping of numerical grids with different topologies is achieved through a modification of both the boundary conditions and through the internal point treatment for those zones where overlapping occurs. The dynamic overlapping grids method allows for an easy and accurate handling of complex geometries. Chimera technique requires to locate regions among different blocks from where extracting an approximation of the solution; it requires to find the so-called donor cells. Once the donor is identified, a convex set of eight donor cell centers is sought and a tri-linear interpolation is used to transfer the solution to the block under analysis. If overlapping cells are found, one of them will be marked as a hole only if the donor cell is smaller. Unlike standard chimera approaches, the cells marked as holes are not removed from the computation; instead, the interpolated solution is enforced on the marked cell point by adding a forcing term to the Navier-Stokes equations, in a body-force fashion (for more details see (Muscari et al., 2006)), providing good global stability to the whole approach also when the overlapping cells are very different in skewness and dimensions.

High performance computing capabilities are obtained with an efficient shared and distributed memory parallelization (Broglia et al., 2014).

Figure 5 shows a sketch of the mesh adopted for all the benchmarks: different blocks are designed, the finest one consisting of a polar mesh around the cylinder.

In order to correctly capture the velocity derivatives inside the boundary layer, block $N°1$ presents a radial stretching of the numerical cells. The spatial discretization on the cylinder is $d/\Delta r \simeq 1260$, here Δr represents the length of the smallest side of the computational cell. The block $N°2$ is an uniform Cartesian mesh with $d/\Delta r \simeq 50$ designed to correctly capture the cylinder near-wake as well as the high deformation of the free surface expected within this region. In the other mesh-blocks, the resolution is degraded in order to save the CPU time costs. The total number of computational cells is about 187,000.

The time step is set as $\Delta t U/d = 10^{-3}$ in order to follow the rapid movements of the free surface in the neighborhood of the cylinder. Indeed, the advection CFL factor ($\Delta t\, U/\Delta r$) is of order 0.1 in this part of the domain.

4.3. ANSYS Fluent code: two-phase Finite Volume Method with Volume of Fluid technique (VOF-FVM)

For the third computational model adopted, again the incompressible Navier-Stokes equations are solved using a Finite Volume Method. However, for this last solver a two-phase model is adopted. The density ratio between the liquid and the gaseous phase is equal to 1000 (like the water/air density ratio) with the gas treated as incompressible.

The code is the widely used commercial software ANSYS Fluent (Ansys, 2013). A Volume-of-Fluid (VOF) technique is used by ANSYS Fluent to track the air/water interface evolution, and in particular, a Geo-Reconstruct technique is used to track the free-surface position, rendering a piecewise linear reconstruction of the interface. For the discretization of time derivatives, an implicit first order backward differencing scheme is used. Regarding the spatial discretization, the third order QUICK (Quadratic Upstream Interpolation for Convective Kinematics) scheme has been selected.

In Figure 6, a sketch of the mesh adopted is depicted. The total number of computational cells in the liquid and gas domains is 335,000. Many of these cells are in the gas domain and therefore are hardly useful. Indeed, the mesh adopted is structured and also this aspect leads to the existence of a substantial number of cells in regions of the fluid domain where the solution is practically unperturbed. Conversely, the Xnavis solver mesh is characterized by about one half of the elements, being the chimera technique able to concentrate the greatest part of them in the near-field and in the wake regions.

The central part of the mesh is stretched in order to increase the resolution in the boundary layer regions. Using this simple mesh, the resolution $d/\Delta r$ passes from 1200 on the cylinder surface down to 200 when reaching the free surface

over the cylinder. In the wake region, the resolution degrades to 50 (again Δr represents the length of the smallest side of the computational cell). The above ratios are quite similar to the ones of Xnavis, although for the latter solver, the mesh is better adapted thanks to the Chimera technique.

The time step adopted is $\Delta t U/d = 1.25\,10^{-3}$, leading to advection CFL factors ($\Delta t\, U/\Delta r$) of order 1 in the boundary layer region and of order 0.1 in the region close to the free surface. These numbers are similar to the ones of the LS-FVM solver.

ANSYS Fluent has been recently used to compute forces on submerged cylinders combining waves and current, using, as in present work, a two-dimensional approach (Bai et al., 2017). Bai et al. (2017) compared their simulations with experiments carried out at $Re \approx 12000$, finding fair agreement, a fact that provides further evidence on the findings of Sheridan et al. (1997) regarding the prevalent two-dimensionality of the flow, even at those intermediate Reynolds numbers.

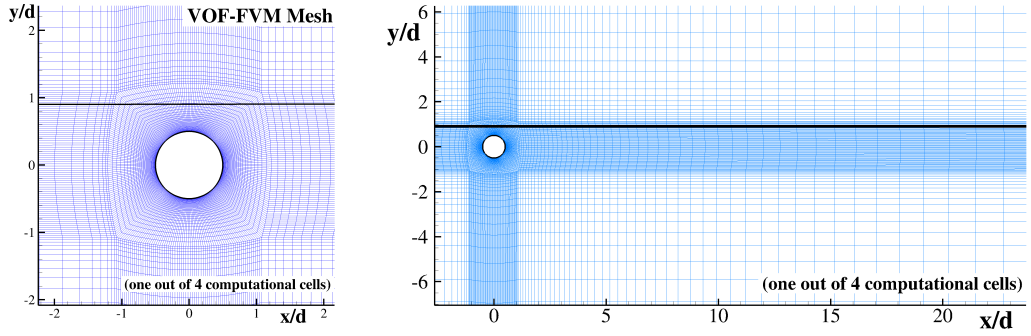

Figure 6: Sketch of the mesh used with the VOF-FVM solver. Each cell on the figure represents 4x4 computational cells. The total number of computational cells is 335,000. The horizontal line represents the undisturbed air/water interface.

5. Preliminary test on unbounded condition: comparison among FVM and δ^+-SPH against DVH

In order to test the solvers with the parameters and the time-space discretizations selected, the unbounded condition is considered first. In this condition, the Reynolds number (set again to $Re = 180$) is the only dimensionless number of the problem .

For this case, the reference solution is generated through the DVH solver. With this Particle Vortex Method, it is possible to resolve with great accuracy the viscous flow past a cylinder, but it is not trivial to include a free-surface boundary, being this topic still under development. Different DVH simulations have been performed to reach a convergent solution. For the finest resolution an uncertainty of 0.5% on the drag and lift peak is obtained. For DVH, the unbounded condition

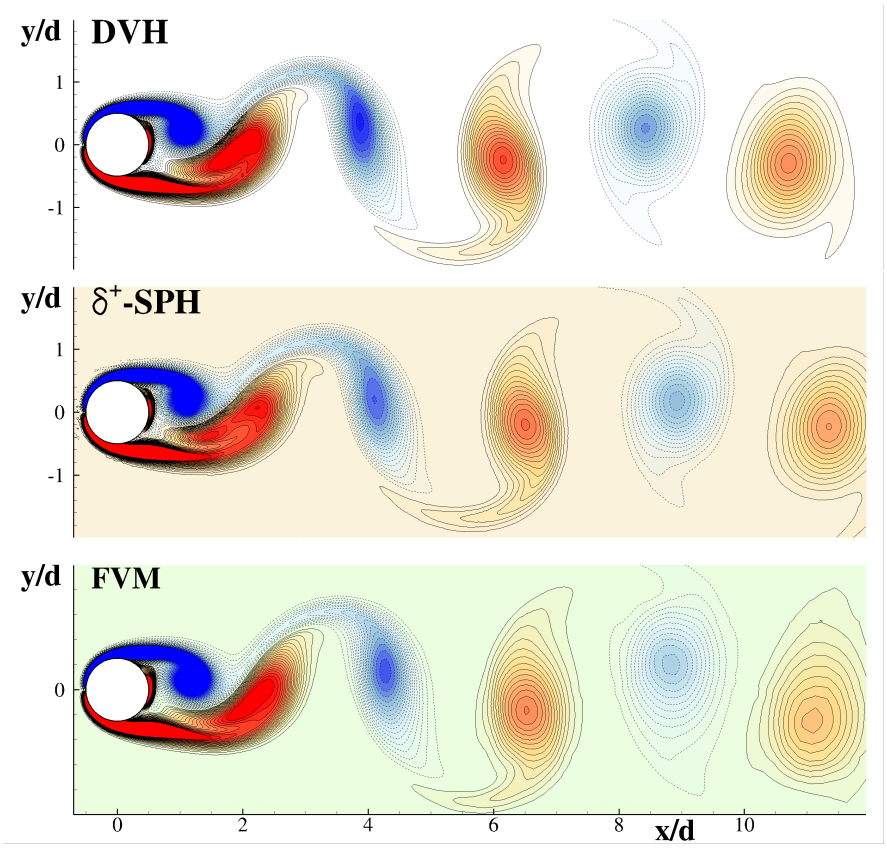

Figure 7: Flow past a circular cylinder, unbounded condition. Vorticity field at maximum of the lift force evaluated by the DVH (left), the δ^+-SPH (middle) and by the FVM solver (right). Dimensionless vorticity $\omega d/U$ scales from -3 (blue) to 3 (red).

is intrinsically satisfied. This is not the case for SPH. For DVH, the $\partial\Omega_F$ boundary is removed and the cylinder is positioned at the center of a closed channel of width $\hat{H}/d = 16$. The latter has been selected in order to get negligible effects of the bottom boundary on the global force acting on the cylinder. The outflow velocity

is now forced to equal the free-stream velocity U, in such a way that the flow-rate guarantees mass invariance in Ω during the simulation. This is an important constraint since, in the present SPH model, a weakly-compressible formulation is assumed. Furthermore, to avoid a finite jump of the particle velocities when passing through $\partial\Omega_O$, a sponge region (where the viscosity is artificially increased) is also applied in this unbounded test.

For the unbounded condition, since the two FVM solvers, Xnavis and ANSYS Fluent, are based on the same approach, only the ANSYS Fluent solver is used.

Figure 7 depicts the vorticity field corresponding to a maximum of the lift during the periodic steady state regime, evaluated with DVH, δ^+-SPH and FVM. As can be seen, the near-field during the von Kármán shedding is very similar for the three solvers. However, in the far-field, the vorticity evaluated by FVM is affected by an evident numerical diffusion related to the mesh stretching. The reader is warned about the background colors used for the zero-level of the vorticity field:

$$\begin{aligned} \delta^+\text{-SPH} &\Rightarrow \textbf{light-red} \\ \text{LS-FVM} &\Rightarrow \textbf{light-blue} \\ \text{VOF-FVM} &\Rightarrow \textbf{light-green} \end{aligned}$$

These choices are also used in the next section.

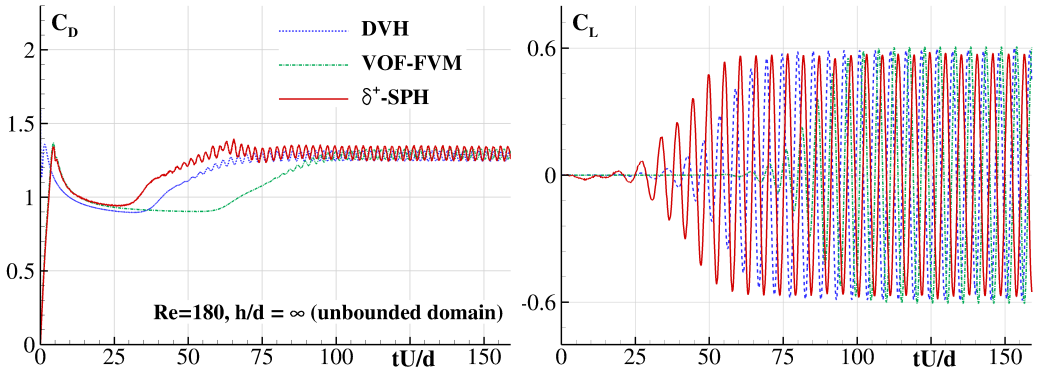

Figure 8: Flow past a circular cylinder, unbounded condition. Drag (left) and Lift (right) coefficients evaluated with DVH (dashed line), δ^+-SPH (solid line), and ANSYS Fluent (dash-dotted line) solvers. All time history files in the paper are downloadable from http://canal.etsin.upm.es/papers/colagrossietalcaf2018/

Figure 8 shows the corresponding time behaviors of the drag and lift coefficients. For the DVH solver, a sudden start of the current is implemented in the code. However, since the comparisons focus on the periodic regime, this different initial condition is not relevant. The inceptions of Von Kármán vortex shedding do not appear at the same time instant for the three solvers. The difference is connected with the spontaneous flow symmetry disruption, numerically triggered in a slightly different way by the three schemes.

When the periodic steady state regime is reached, the comparisons between the three solvers are in a good agreement. In order to give a measure of such comparisons, the mean C_D, the amplitude of C_L and the Strouhal number are reported in Table 1. Although not clearly visible in the left plot of figure 8, the time periods of the drag coefficients are in well agreement similarly to the lift coefficients. The good agreement of the solvers is an indication that the spatial resolutions adopted are suitable also for the three benchmarks in the open-channel flow condition.

	$\overline{C}_D$	C'_L	St
DVH	1.28 ±0.04	0.59	0.187
δ^+-SPH	1.30 ±0.05	0.59	0.191
FVM	1.29 ±0.03	0.61	0.193

Table 1: Flow past a circular cylinder, unbounded condition. Mean Drag coefficients, amplitude of the Lift coefficient C'_L and Strouhal number evaluated by the DVH, δ^+-SPH and ANSYS Fluent solvers.

6. Comparison of the results of LS-FVM, VOF-FVM and δ^+-SPH for the viscous free-surface benchmarks

6.1. Benchmark I (Fr=0.3,h/d=0.4, Re=180)

The first benchmark is characterized by a small interaction between the cylinder wake and the free-surface evolution. As in the unbounded case, the flow quickly tends to a periodic steady state regime, in which the mean lift force is not zero because the flow velocity between the cylinder and the free surface is larger than the one below the cylinder. Furthermore, the vertical force F_y has also a constant buoyancy component B, subtracted when evaluating the lift coefficient:

$$C_L(t) = \frac{F_y(t) - B}{1/2\,\rho\, U^2\, d\, L}, \tag{4}$$

where L is used as unitary span-wise dimension.

Figure 9 depicts the vorticity in the near-field obtained with the three solvers.

The plots are evaluated at three time instants, corresponding respectively to the maximum (top row), the zero (middle row) and the minimum (bottom row) of the lift force. For this problem, a regular shedding (resembling the classic Von Kármán street) with large dipoles arrangement of the flow field develops.

The induced motion of the free surface, even though weak, is characterized by a cyclical formation of spilling wave breaking. The dynamics of the breaking is driven by the oscillation of the upper (negative vorticity) shear layer, which induces a steep wave formation and its final breaking.

The global agreement among the solvers is satisfactory even though the LS-FVM solver seems to produce a stronger interaction with the free surface,

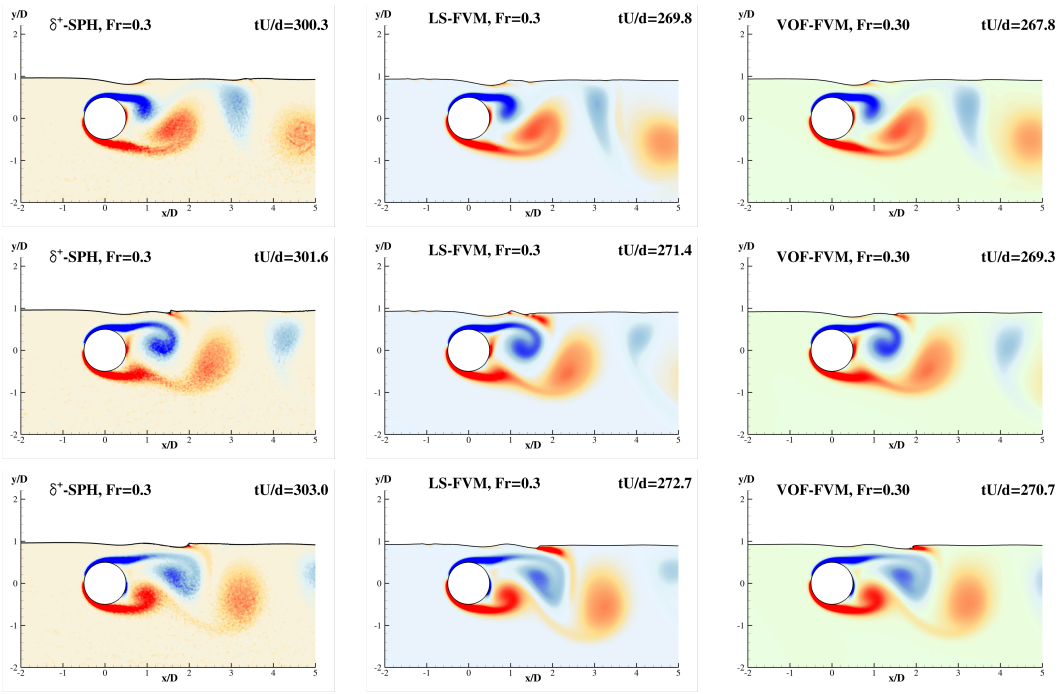

Figure 9: **Benchmark I** : Contour plot of the vorticity in the near-field computed by δ^+-SPH (left), LS-FVM (middle), VOF-FVM (right). The plots correspond to the periodic regime: maximum of the lift force (top row), zero lift force (middle row), minimum of the lift force (bottom row). Dimensionless vorticity $\omega d/U$ scales from -5 (blue) to 5 (red).

detectable on a larger vorticity intensity generated by the spilling breaking (see the bottom row of Figure 9).

Despite the VOF-FVM simulations are with two-phases, the effect of the air seems to be totally negligible in this case, with a complete absence of bubble entrapment, thus justifying the use of one-phase approaches.

Figure 10 shows the time histories of the force coefficients for the initial transient part, $tU/d < 80$, of the simulation. During the acceleration stage, $tU/d \simeq 5$, corresponding to the end of time ramp of the current $U(t)$, the forces evaluated by the different solvers are very close each other. In the subsequent evolution, a precise match is lost because of the non-linear interaction with the free surface.

After the transient stage, a periodic steady state regime is attained, and the forces become basically monochromatic, even if a low frequency modulation on the drag force is visible, likely connected with the influence of the inflow/outflow boundaries, as already commented (see section 2). The two FVM solvers remain more in phase compared to the δ^+-SPH.

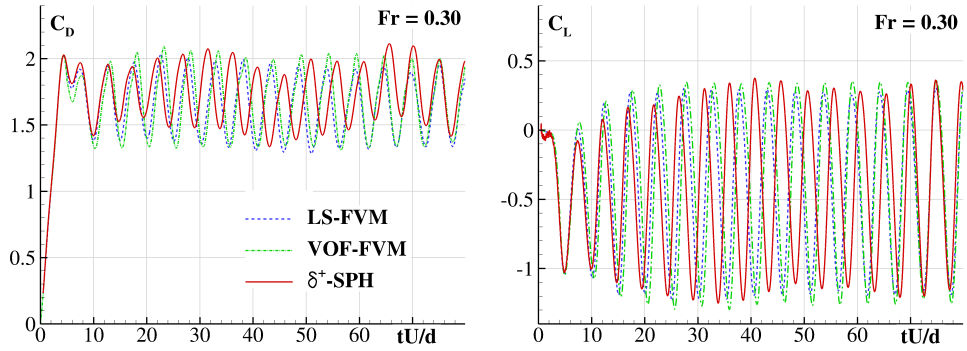

Figure 10: Case Fr = 0.3: cylinder drag (left) and lift (right) coefficients short-time evolution calculated by the three solvers.

	C_D	C_L	St
δ^+ SPH	1.73 ± 0.27	-0.37 ± 0.77	0.209
LS-FVM	1.63 ± 0.29	-0.41 ± 0.74	0.190
VOF-FVM	1.66 ± 0.33	-0.41 ± 0.80	0.192

Table 2: Case Fr = 0.3. Comparison among solvers of force coefficients and Strouhal number.

In Table 2, the mean values, amplitudes and Strouhal numbers output by the three solvers, are reported. As expected, the free surface highly impacts the mean values of the force coefficients compared to their unbounded counterparts (see Table 1 for comparison): the mean lift is not null, and the mean drag coefficient rises up because of the interaction between the shear layers and the free surface.

Despite the good agreement of the vorticity fields, discrepancies among the solvers are detectable when observing the values reported in Table 2. The evaluations given by the two FVM solvers are quite close to each other, while the δ^+ SPH solver overestimates the $\overline{C}_D$ by about 5% with respect to the FVM solvers, and underestimates $\overline{C}_L$ by about 10%. The oscillation amplitudes are in fair agreement for both the force coefficients. The lift amplitude C'_L presents a maximum deviation of 4%, while for the C'_D, this is about 22% (note that C'_D is about one tenth of $\overline{C}_D$). The Strouhal numbers obtained from the FVM codes signals are very close to each other, whereas a discrepancy of 10% (greater) is experienced by the SPH solver.

6.2. Benchmark II (Fr=1.0, h/d=0.4, Re=180)

In the present subsection, the case with Fr = 1.0 is considered. In this case, the interaction with the free surface is rather intense, especially in the transient phase.

Figure 11 depicts the evolution of the free surface and the vorticity at six time instants, evaluated with the three solvers. The first five time instants correspond to the transient stage, $tU/d < 12$, while the last corresponds to the flow field for a regime (long-time) condition at $tU/d = 150$.

Again, the solvers are in fair agreement, even though some discrepancies, related to the different approaches, are noticeable. In the first time instant shown, $tU/d = 4.0$, when the free surface deforms because of the pressure drop right past the cylinder, there are not appreciable differences among the solvers.

At $tU/d = 6.0$, the deformation of the free surface leads to the formation of a first small breaking event, followed by a greater plunging jet, at time $tU/d = 8.2$. The evolution of the latter leads to a splash-up, evident at time instants $tU/d = 10$ and $tU/d = 12$. All the solvers are able to capture these flow features even if noticeable geometrical differences appear. Nonetheless, the vorticity fields obtained by the three codes are very similar in shape and intensity. Starting from $tU/d = 10$, differences between the VOF-FVM solution and the other two solvers become more evident. Indeed, the VOF-FVM solution is based on a two-phase model, and therefore, the breaking events induce entrapment of air bubbles. Conversely, the δ^+-SPH and the LS-FVM are based on a single-phase model, and

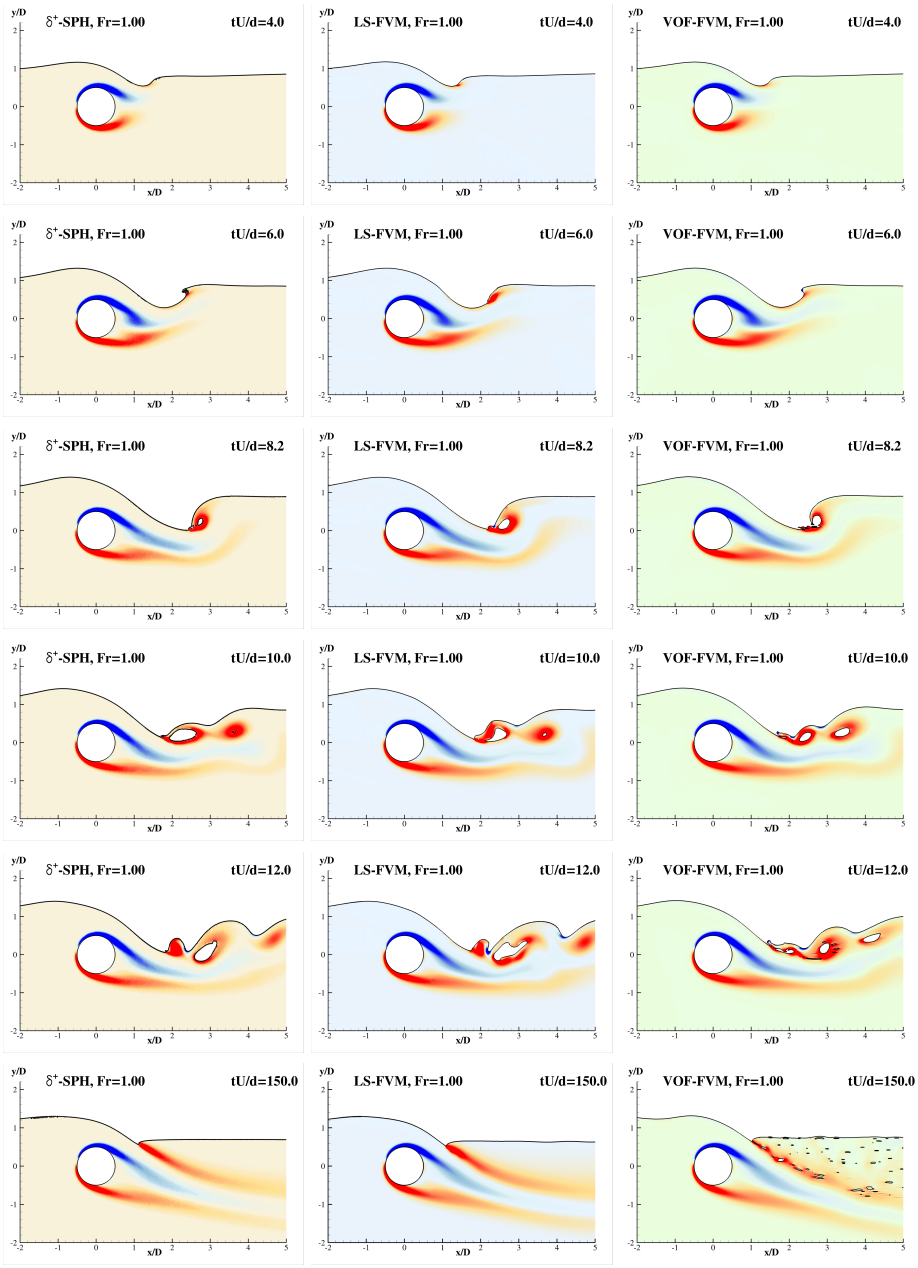

Figure 11: **Benchmark II** : Contour plot of the vorticity in the near-field computed by δ^+-SPH (left), LS-FVM (middle), VOF-FVM (right). The first five rows show the transient regime while the bottom row corresponds to the long-time evolution. Dimensionless vorticity $\omega d/U$ scales from -5 (blue) to 5 (red).

	C_D	C_L
δ^+ SPH	1.23 ± 0.002	-0.39 ± 0.002
LS-FVM	1.25 ± 0.019	-0.43 ± 0.020
VOF-FVM	1.16 ± 0.016	-0.38 ± 0.019

Table 3: Case Fr = 1. Comparison among solvers of force coefficients.

hence, during the breaking processes, empty cavities are formed, that collapse during the subsequent time evolution.

In spite of the strong unsteadiness characterizing the initial part of the time evolution, an almost steady state is reached for $tU/d > 100$. The bottom row of Figure 11 refers to the near-field at $tU/d = 150$. The agreement is evident for the SPH and the LS-FVM solvers, with the presence of a stable spilling breaking behind the cylinder, which determines a stable shear layer of positive vorticity. The Von Kármán shedding is completely inhibited in this benchmark. Looking at the VOF-FVM solution at $tU/d = 150$ (right plot of the bottom row of Figure 11), many air bubbles are entrapped by the spilling breaking in the recirculation region. On the other hand, despite the presence of the air-bubbles cloud, the vorticity field obtained through the VOF-FVM is very similar to the δ^+-SPH and LS-FVM ones. From the above results, it may be concluded that the differences between a single-phase and a two-phase model are not relevant for this Benchmark. A further confirmation is given by the analysis of the time histories of the force coefficients.

Figure 12 depicts the force coefficients time histories output by the three solvers. In Table 3, the mean values of force coefficients, calculated by averaging the quantities in the time interval $tU/d \in (300, 500)$, are collected together with their standard deviations. Although the $\overline{C}_D$ calculated by LS-FVM and δ^+-SPH one are very similar, VOF-FVM about 7% smaller. Conversely, when looking at the lift coefficient, the $\overline{C}_L$ of VOF-FVM is superimposed on the δ^+-SPH one, while the LS-FVM $\overline{C}_L$ is about 10% lower.

It is evident from the plots of Figure 12 that the δ^+ SPH time signals are more stable than the solutions provided by the two FVM solvers. This is reflected on the low standard deviation values reported in Table 3 for δ^+ SPH. At the present stage, a conclusive explanation for such an effect is missing, even though one may suspect to be connected to the in-outflow conditions, or to the ability of the δ^+ variant of the particle solver in guaranteeing a more stable flow with respect to mesh-based solvers. A more in depth-investigation on this topic will be matter of future works.

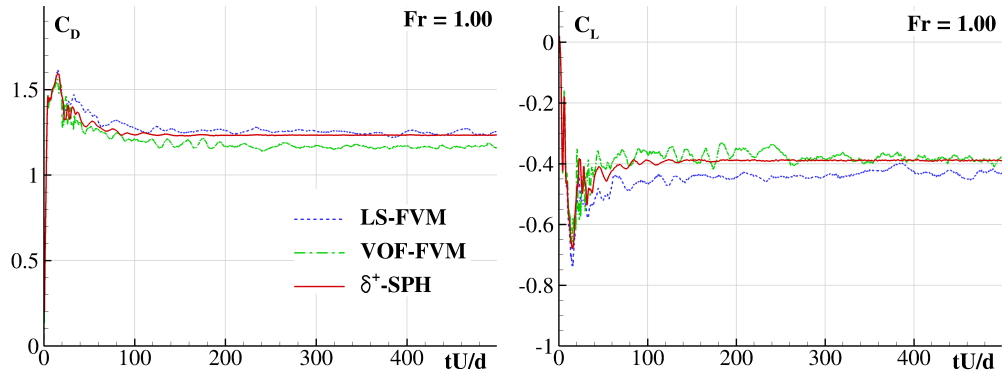

Figure 12: Case Fr = 1: time histories of the cylinder drag (left) and lift (right) coefficients calculated by three solvers.

6.3. Benchmark III (Fr=0.55,h/d=0.4, Re=180)

If ranked by increasing Froude number, this should have been the second case. However, it is left as the last one as it has been found to be the most challenging, involving the so-called "metastable" regime. Such regime consists of a continuous switch of the flow behavior, where the Von Kármán shedding is periodically excited and inhibited.

Similarly to the previous test-case, we start by comparing the near-fields given by the three solvers in the transient stage. Figure 13 shows the vorticity fields for five time instants in the time range $tU/d \in [5, 18]$. Likewise the Benchmark II, the flow is again characterized by the formation of a breaking wave, whereas, at the last time instant $tU/d = 18$ (bottom row of Figure 13), a stable spilling breaking takes place and the flow seems to reach an almost steady state. The solutions of the three solvers are quite similar, although, as for the Benchmark II, the VOF-FVM exhibits the entrapment of air bubbles with again negligible influence on the vorticity field.

In Figure 14, where the long-time evolution is depicted, four time instants are reported and highlighted on the bottom plot with the capital letters A,B,C and D. The "metastable" behaviour becomes clear when the plots on the first row are compared to the other three. The weak oscillation of the shear layers shown in the case A, becomes more intense at later instants B, C, D, for which a full Von Kármán shedding takes place, equivalently to Benchmark I. During this stage, the free surface is highly affected by the underlying shear layers dynamics, with the formation of plunging breaking waves.

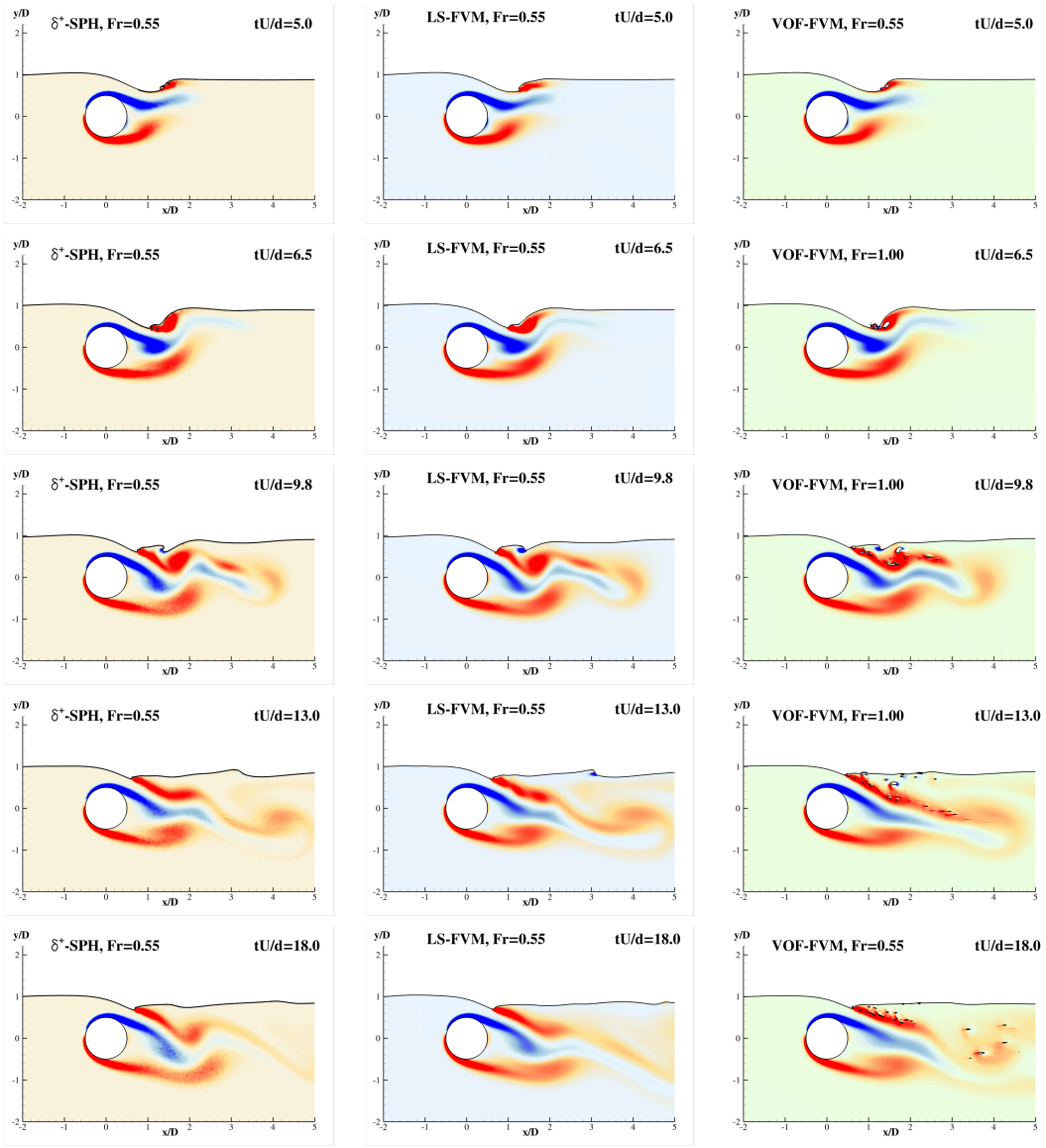

Figure 13: **Benchmark III**: Contour plot of the vorticity in the near-field computed by δ^+-SPH (left), LS-FVM (middle), VOF-FVM (right). The plots correspond to the transient stage. Dimensionless vorticity $\omega d/U$ scales from -5 (blue) to 5 (red).

These changes induce large variation on the forces; in the bottom plot of Figure 14 a time history of the lift force is reported. When the Von Kármán

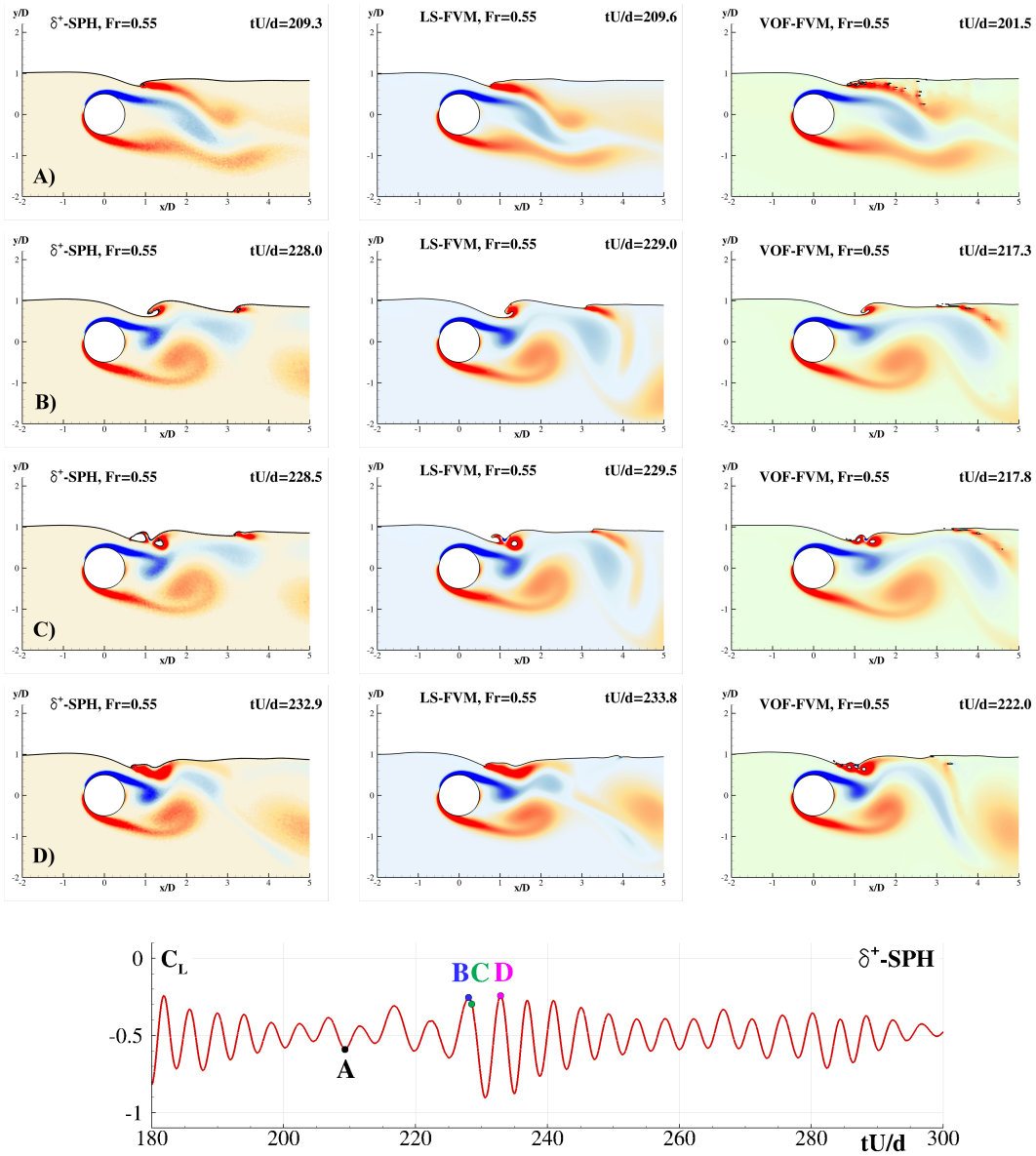

Figure 14: **Benchmark III**: Contour plot of the vorticity in the near-field computed by δ^+-SPH (left), LS-FVM (middle), VOF-FVM (right). The plots correspond to the metastable regime. Dimensionless vorticity $\omega d/U$ scales from -5 (blue) to 5 (red). Bottom plot: time history of the δ^+-SPH lift coefficient, capital letters and dots refer to the four time instants selected for the vorticity plots.

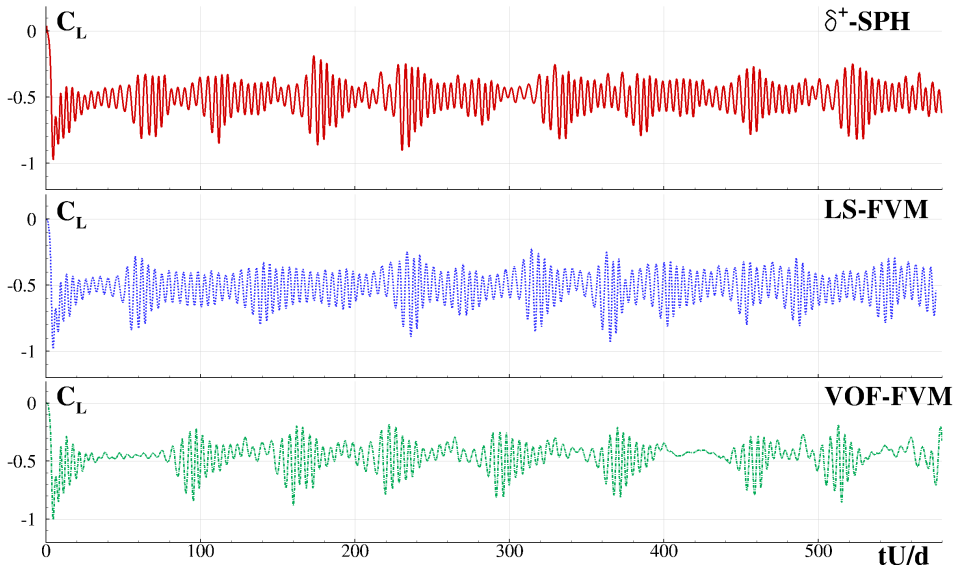

Figure 15: Case Fr = 0.55. Lift coefficient time evolution calculated by the three solvers.

shedding is excited, the intensity of the lift force increases, as exemplified by the points corresponding to instants B,C and D.

Analogously to the the vorticity fields, the free-surface shape is similar for the three algorithms.

It is worth noticing that the time instants selected for the Figure 14 are not the same for the three solvers, the reason being that the flow alternate states (i.e. Von Kármán shedding inhibited or excited) develop in slightly different time ranges.

This point is better appreciated in the plots in Figure 15, where the time histories of the lift forces recorded by the three solvers are displayed. All the three signals present a fundamental frequency linked to the Von Kármán shedding and a low frequency modulation. The fundamental frequency, in the right column of Table 4, is in fair agreement among the solvers.

Conversely, the modulation appears quite irregular, being the metastable regime driven by a complex non-linear interaction between the cylinder wake and the breaking events of the free surface. In particular, the amplitudes of the low frequency modulations predicted by the δ^+-SPH and by the two FVM solvers appear quite different. The VOF-FVM solver shows the higher amplitude, where the modulation is so intense that during some time intervals the oscillatory shedding is totally nullified. Conversely, the LS-FVM shows a weaker modulation, while the δ^+-SPH exhibits a modulation with an intermediate

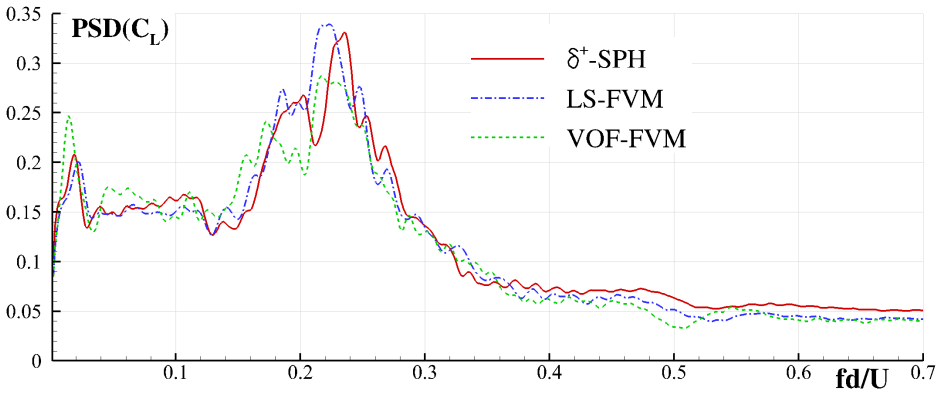

Figure 16: Case Fr = 0.55. Power Spectral Density (PSD) of the lift coefficient time histories for the three different solvers.

intensity between the two FVM solvers, but closer to the LS-FVM, something we attribute to the fact that the LS-FVM and the δ^+-SPH implementations solve single-phase models while the VOF-FVM is solving multiphase incompressible. Confirming this hypothesis remains as future work.

The Fourier transform of the lift coefficient for this case, smoothed to remove the oscillations induced by the finite duration of the time series, is presented in Fig. 16. Consistently with previous appreciations referred to the time histories, most of the energy is located in the main shedding range (Strouhal number around 0.2) but a non-negligible amount of energy is also present in the low frequency range (Strouhal number around 0.02). A larger similitude between LS-FVM and δ^+-SPH is also noticeable in the spectra.

The modal (fundamental) value of the main harmonics and subharmonics, together with their ratio are included in Table 4. This ratio is consistently of order 10 in our analysis, compared to (Sheridan et al., 1995), who report this value to be of order 100 in their experiments, with much larger Reynolds number and of course the inherent surface tension

The mechanism underlying those differences among the solvers seems hard to understand, since, as shown above, sensible differences on the different near-fields are not evident and, for sure, do not allow to justify the discrepancy on the forces acting on the cylinder. As shown by Colagrossi et al. (2017b), by using the ANSYS Fluent solver and by changing the spatial resolution, the time steps and the distance of the cylinder from the to inflow/outflow boundaries, the lift time

	C_D	C_L	St_1	St_2	St_1/St_2
δ^+ SPH	1.43 ± 0.31	-0.50 ± 0.11	0.236	0.018	≈ 13
LS-FVM	1.36 ± 0.26	-0.51 ± 0.12	0.224	0.022	≈ 10
VOF-FVM	1.48 ± 0.22	-0.46 ± 0.11	0.217	0.014	≈ 15

Table 4: Case Fr = 0.55. Comparison among solvers of force coefficients and Strouhal number. St_1 stands for the modal value in the range of the vortex shedding while St_2 refers to the modal value in the subharmonic range.

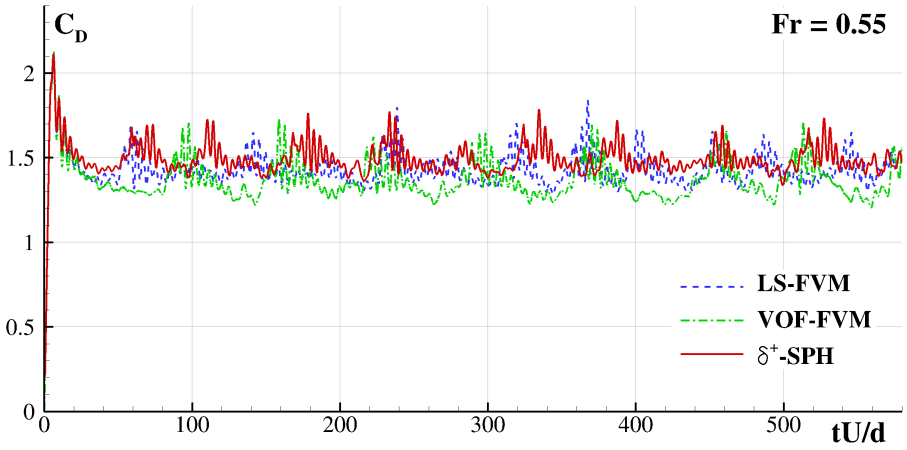

Figure 17: Case Fr = 0.55. Drag coefficient time evolution calculated by the three solvers.

history spectra can significantly change.

In Figure 17, the time histories of the drag coefficients calculated by the three codes are plotted. Also for the C_D a low frequency modulation is rather visible.

Similarly to the Benchmark II, the mean values of the force coefficient and the standard deviation evaluated in the time range $tU/d \in (300, 600)$ are reported in Table 4. Surprisingly, despite the discussed differences among the time behaviors, the mean values of the global forces and their standard deviations show fair agreement. A maximum difference of 8.8% between VOF-FVM and LS-FVM is appreciated on the mean $\overline{C}_D$ and, similarly, of 9.8% between the same solvers on $\overline{C}_L$. Regarding the drag coefficient, the standard deviation of the δ^+ SPH's is larger than the LS-FVM's (16%) and the VOF-FVM's (29.5%), whereas the lift coefficients show almost identical standard deviations.

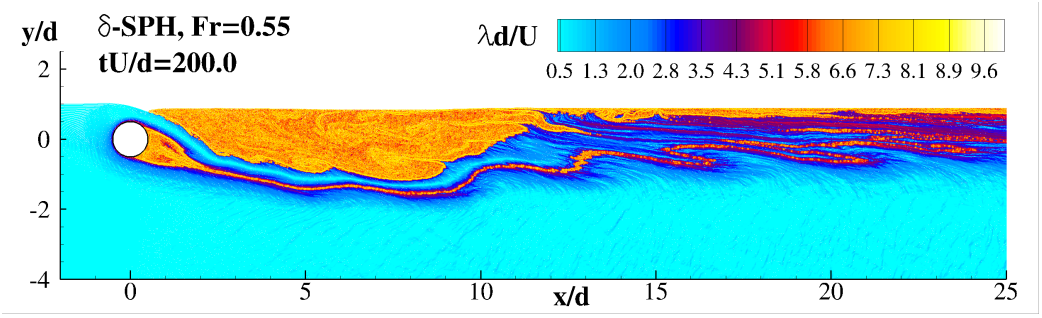

Figure 18: Benchmark III. Lyapunov exponent evaluated by the δ-SPH scheme.

7. δ-SPH versus δ^+-SPH: relevance of the Shifting technique for capturing the meta-stable condition

Motivated by this paper aiming to contribute to the Computers & Fluids "Special issue on Theoretical, numerical and computational advances of the SPH method for solving fluid problems", a dedicated analysis has been carried out regarding the effect of the improvements that the δ^+ variant of the SPH formulation SPH solver has on the performance and accuracy of the solver.

In previous sections, it has been shown that the δ^+-SPH model is able to provide results in qualitative and fair quantitative agreement with those output by the Finite Volume Methods. In (Bouscasse et al., 2017), it was remarked that the δ-SPH can also be used for this kind of viscous free-surface flows. However, after a more detailed analysis, it has been found that the results for the Benchmark III provided by the δ-SPH are dramatically different than the solutions presented in subsection 6.3.

Figure 18 shows the contour plot of the Lyapunov exponents obtained with the δ-SPH for the Benchmark III. As it can be seen, the flow pattern is more similar to the one of the Benchmark II, rather than to the flow pattern related to the metastable condition.

Looking at the force coefficient time histories of Figure 19, it is evident that, after the transient stage, the δ-SPH reaches an almost steady state, thus implying that the metastable mode is absent and that the wake does not present any relevant oscillations in the near-field.

Figure 20 depicts an enlarged view of the flow field behind the cylinder. The left plot corresponds to δ-SPH while the right one to δ^+-SPH, both at $tU/d = 213$. The distribution of particles appears quite irregular for the former, especially in

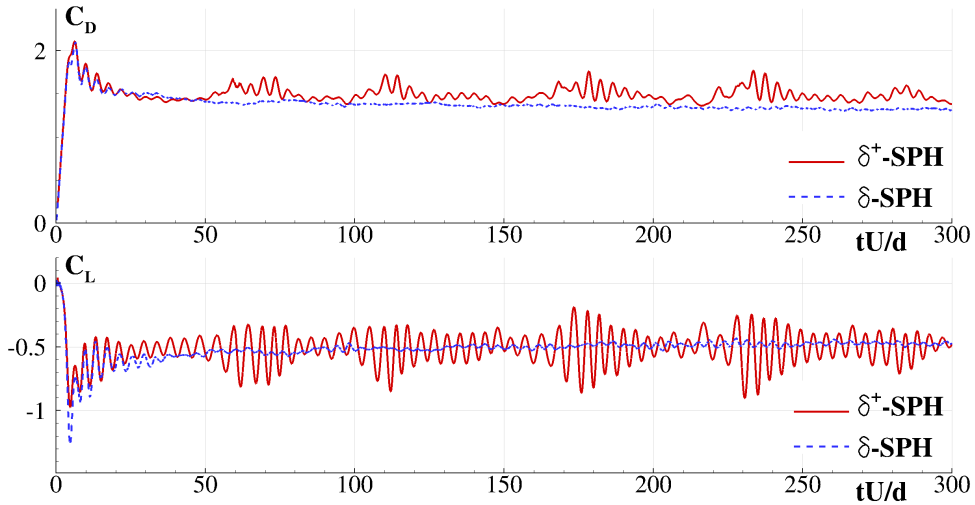

Figure 19: Benchmark III. Time histories of the Drag (top) and Lift (bottom) coefficients calculated by δ^+-SPH (solid line) and δ-SPH (dashed line).

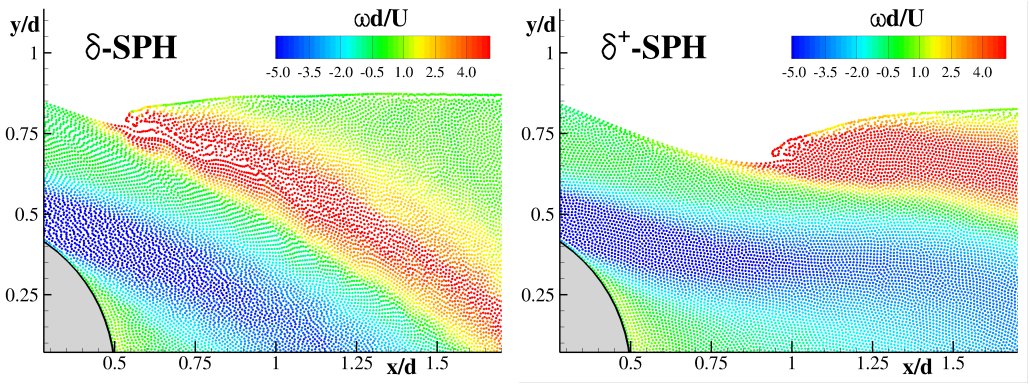

Figure 20: Benchmark III. Enlarged view of the particles distributions behind the cylinder at dimensionless time $tU/d = 213$. The colors are representative of the vorticity field evaluated by δ-SPH (left) and by δ^+-SPH (right).

the neighborhood of the spilling breaking wave. This is not the case for δ^+-SPH, for which the Particle Shifting Technique assumes a crucial role in regularizing the particle distribution. Because of the noisy particle distribution, also the δ-SPH vorticity field is more irregular with respect to the one evaluated with δ^+-SPH (the reader interested on this issue is referred to Khayyer et al. (2017); Gotoh and Khayyer (2018)). On top of these differences, it also appears that the δ-

SPH solution predicts a jet-flow over the cylinder with a larger steepness than the one obtained using a particle shifting technique. This is a key-point since the metastable model is possible only if the jet-flow over the cylinder is almost horizontal.

In order to better understand the relevance of the results rendered by δ-SPH for Fr $= 0.55$ and $h/d = 0.4$, a series of tests with Fr and h/d around such reference values were run. The specific objective as to to check whether a metastable condition could be captured by this SPH model. However, for none of the tests performed, not discussed for the sake of brevity in detail in this work, the metastable states appeared.

As a final reflection for this section, the results reported are an interesting example of how the test-cases suggested in this work can be useful for validating other CFD solvers.

8. Conclusions

The research question motivating this paper has been whether it is possible to set relevant, robust and reliable benchmarks for viscous free-surface flows with complex free-surface dynamics. The method proposed for finding the answer to this question has consisted of selecting three conditions leading to increasing flow complexity, and to simulate them using three well established solvers, based on diverse numerical techniques, namely δ^+-SPH and Finite Volume Method, the latter with either Level-Set or Volume-of-Fluid algorithms to track the free surface.

Three different solvers, based on those approaches, have been compared through benchmarks of increasing complexity, established on the common problem of a submerged horizontal cylinder in an uniform current perpendicular to its axis, with the Froude number taking the values 0.3, 1.0 and 0.55, and the submergence ratio being set as 0.4, i.e. with the cylinder close to the undisturbed free surface.

In the first two benchmarks, i.e. with Froude numbers 0.3 and 1.0, the solvers have shown fair agreement in forces and vorticity fields, both during the periodic steady state and also during the initial transient stages. In particular, the benchmark II (Fr = 1.0) has evidenced that the single or two-phase approaches do not affect the agreement between the three numerical models.

The last case, with Froude number equal to 0.55, has revealed to be the most challenging due to the onset of the so-called two metastable states in the cylinder wake, in which the negative vorticity tongue either remains horizontal, thus

blocking the shedding of alternate vortices, or gets projected downstream, leading to alternate shedding and an unsteady free-surface dynamics with breaking. The periodic switch between these states leads to the presence of a low frequency harmonic in the time-histories of the force coefficients. This phenomenon had been previously described in experiments at a larger Reynolds number and in simulations but quantitative related measures were missing.

In this benchmark, the three solvers are able to capture the metastable dynamics and output similar mean values for the force coefficients. However, the choice of the numerical approach seems to slightly affect the time behavior of the global forces, particularly the intensity and frequency of the referred subharmonic. In any case, the three solvers output a subharmonic frequency with Strouhal numbers around 0.02, which makes the ratio between the main harmonic frequency and the subharmonic to be consistently of order 10. This result can serve as reference for other solvers and opens the question of how it depends on the parameters in hand, namely Reynolds number, Froude number and submergence ratio.

For this particular case (Fr = 0.55, $h/d = 0.4$), motivated by this paper aiming to contribute to the Computers & Fluids "Special issue on Theoretical, numerical and computational advances of the SPH method for solving fluid problems", a dedicated analysis has been carried out regarding the effect of the improvements that the δ^+ variant of the SPH formulation has on the performance and accuracy of the solver. It has been shown that particle shifting, incorporated in the δ^+ variant, is indispensable for capturing the metastable states dynamics, thus becoming necessary for approaching the kind of problems treated in the paper. This seems to the authors an important outcome of the present research for SPH practitioners.

Overall, the benchmarks proposed can be considered, first, relevant, as they deal with the flow around cylinders, one of the most representative configurations in Engineering Fluid Mechanics; they can be considered, second, robust, since, together, they encompass a family of related flows wide enough to be comparable with solutions from multiple solvers; finally, the benchmarks can be considered reliable because they include solutions obtained with well established solvers that display the same qualitative features, and similar enough quantitative outcomes related to local and global quantities.

Considering these points, the benchmarks can be useful for the hydraulic, marine, and coastal engineering CFD communities, providing them with reference data for the validation of single and multi-phase Navier-Stokes solvers adopted in these contexts. At the same time, small but noticeable local and global differences are present, originated by the difficulties of the numerical methods to capture the

highly non-linear interactions between the vortex wake and the free surface. A better understanding of these difficulties, together with a number of side aspects referred in the text, are left for future work.

Acknowledgements

The numerical computations presented here have been performed with the support of the Super Computing Applications and Innovation (SCAI) department of the CINECA consortium. The authors acknowledge the CINECA award under the ISCRA initiative (with project name "Evaluation of the free-surface instabilities due to the flow past a submerged circular cylinder"), for the availability of high performance computing resources and support.

The SPH simulations performed under the present research have been obtained using the SPH-flow solver, software developed within a collaborative consortium composed of Ecole Centrale de Nantes, NEXTFLOW Software company and CNR-INSEAN.

The contribution concerning VOF-FVM simulations by ANSYS Fluent has been granted by BSHC project "Advanced hydrodynamic research on marine engineering facilities under real environment" within the annual research program of the Institute of Metal Science and Technologies with Hydrodynamic Centre "Akad. A. Balevski", Bulgarian Academy of Sciences

References

Ansys. *ANSYS Fluent Theory Guide (Release 15.0)*. ANSYS, Inc., November 2013.

M. Antuono, A. Colagrossi, S. Marrone, and C. Lugni. Propagation of gravity waves through an SPH scheme with numerical diffusive terms. *Computer Physics Communications*, 182(4):866–877, 2011.

M. Antuono, A. Colagrossi, and S. Marrone. Numerical diffusive terms in weakly-compressible SPH schemes. *Computer Physics Communications*, 183(12): 2570–2580, 2012.

F. Aristodemo, G. Tripepi, D.D. Meringolo, and P. Veltri. Solitary wave-induced forces on horizontal circular cylinders: Laboratory experiments and SPH simulations. *Coastal Engineering*, 129:17–35, 2017.

J. Bai, N. Ma, and X. Gu. Study of interaction between wave-current and the horizontal cylinder located near the free surface. *Applied Ocean Research*, 67: 44–58, 2017.

J. Bonet and M.X. Rodriguez-Paz. Hamiltonian formulation of the variable-h SPH equations. *J. Comp. Phys.*, 209:541–558, 2005.

B. Bouscasse, A. Colagrossi, S. Marrone, and M. Antuono. Nonlinear water wave interaction with floating bodies in SPH. *Journal of Fluids and Structures*, 42: 112–129, 2013.

B. Bouscasse, A. Colagrossi, S. Marrone, and A. Souto-Iglesias. SPH modelling of viscous flow past a circular cylinder interacting with a free surface. *Computers & Fluids*, 146:190–212, 2017.

R. Broglia and D. Durante. Accurate prediction of complex free surface flow around a high speed craft using a single-phase level set method. *Computational Mechanics*, pages 1–17, 2017.

R. Broglia, S. Zaghi, R. Muscari, and F. Salvadore. Enabling hydrodynamics solver for efficient parallel simulations. In *High Performance Computing & Simulation (HPCS), 2014 International Conference on*, pages 803–810. IEEE, 2014.

L. Chiron, S. Marrone, A. Di Mascio, and D. Le Touzé. Coupled SPH-FV method with net vorticity and mass transfer. *Journal of Computational Physics*, to appear on, 2018a.

L. Chiron, G. Oger, M. De Leffe, and D. Le Touzé. Analysis and improvements of Adaptive Particle Refinement (APR) through CPU time, accuracy and robustness considerations. *Journal of Computational Physics*, 354:552–575, 2018b.

A. Colagrossi, D. Durante, J. Bonet Avalos, and A. Souto-Iglesias. Discussion of stokes' hypothesis through the smoothed particle hydrodynamics model. *Physcal Review E*, 96:023101, 2017a. doi: 10.1103/PhysRevE.96.023101.

A. Colagrossi, G. Nikolov, D. Durante, P.N. Sun, and A. Souto-Iglesias. Viscous flow past a circular cylinder close to a free surface: results from a benchmark between SPH and mesh-based solvers. In *12th International SPHERIC SPH Workshop*, 13-15 June 2017b.

A. Di Mascio, R. Broglia, and R. Muscari. On the application of the single-phase level set method to naval hydrodynamic flows. *Computers & Fluids*, 36(5): 868–886, 2007. ISSN 0045-7930. doi: 10.1016/j.compfluid.2006.08.001.

A. Di Mascio, R. Broglia, and R. Muscari. Numerical simulations of viscous flow around a naval combatant in regular head waves. In *Proceedings of the 6th Osaka Colloquium on Seakeping and Stability of Ships*, 2008.

A. Di Mascio, R. Broglia, and R. Muscari. Prediction of hydrodynamic coefficients of ship hulls by high-order Godunov-type methods. *Journal of Marine Science and Technology*, 14(1):19–29, 2009. ISSN 0948-4280. doi: 10.1007/s00773-008-0021-6.

D. Durante, E. Rossi, A. Colagrossi, and G. Graziani. Numerical simulations of the transition from laminar to chaotic behaviour of the planar vortex flow past a circular cylinder. *Communications in Nonlinear Science and Numerical Simulation*, 48:18–38, 2017.

I. Federico, S. Marrone, A. Colagrossi, F. Aristodemo, and M. Antuono. Simulating 2D open-channel flows through an SPH model. *European Journal of Mechanics-B/Fluids*, 34:35–46, 2012.

J.M. Gimenez and L.M. González. An extended validation of the last generation of particle finite element method for free surface flows. *Journal of Computational Physics*, 284:186–205, 2015.

J.M. Gimenez, D.E. Ramajo, S. Márquez Damián, N.M. Nigro, and S.R. Idelsohn. An assessment of the potential of PFEM-2 for solving long real-time industrial applications. *Computational Particle Mechanics*, 4(3):251–267, Jul 2017.

H. Gotoh and A. Khayyer. On the state-of-the-art of particle methods for coastal and ocean engineering. *Coastal Engineering Journal*, 60(1):79–103, 2018.

L. Hernquist and N. Katz. TreeSPH: A Unification of SPH with the Hierarchical Tree Method. *Astrophysical Journal Supplement*, 70:419–446, 1989.

C. W. Hirt and B. D. Nichols. Volume of fluid (VOF) method for the dynamics of free boundaries. *Journal of Computational Physics*, 39(1):201–225, 1981.

A. Khayyer, H. Gotoh, and Y. Shimizu. Comparative study on accuracy and conservation properties of two particle regularization schemes and proposal of

an optimized particle shifting scheme in isph context. *Journal of Computational Physics*, 332:236 – 256, 2017.

S. Khorasanizade and J.M.M. Sousa. An innovative open boundary treatment for incompressible SPH. *International Journal for Numerical Methods in Fluids*, 80:161–180, 2016.

M. Landrini, A. Colagrossi, M. Greco, and M.P. Tulin. The fluid mechanics of splashing bow waves on ships: A hybrid BEM-SPH analysis. *Ocean Engineering*, 53(0):111–127, 2012.

M. Lastiwka, M. Basa, and N.J. Quinlan. Permeable and non-reflecting boundary conditions in SPH. *International Journal for Numerical Methods in Fluids*, 61 (7):709–724, 2008.

S. J. Lind, R. Xu, P. K. Stansby, and B. D. Rogers. Incompressible smoothed particle hydrodynamics for free-surface flows: A generalised diffusion-based algorithm for stability and validations for impulsive flows and propagating waves. *Journal of Computational Physics*, 231(4):1499–1523, 2012. doi: 10.1016/j.jcp.2011.10.027. URL https://www.scopus.com/inward/record.uri?eid=2-s2.0-84855197493&doi=10.1016%2fj.jcp.2011.10.027&partnerID=40&md5=3daf95bb1061a213ccadda550af3a0c4. cited By 56.

S. Marrone, A. Colagrossi, M. Antuono, G. Colicchio, and G. Graziani. An accurate SPH modeling of viscous flows around bodies at low and moderate Reynolds numbers. *Journal of Computational Physics*, 245:456–475, 2013.

D. Molteni, R. Grammauta, and E. Vitanza. Simple absorbing layer conditions for shallow wave simulations with Smoothed Particle Hydrodynamics. *Ocean Engineering*, 62:78–90, 2013.

J. Monaghan and R. A. Gingold. Shock Simulation by the particle method SPH. *Journal of Computational Physics*, 52(2):374–389, 1983.

R. Muscari, R. Broglia, and A. Di Mascio. An overlapping grids approach for moving bodies problems. In *The Sixteenth International Offshore and Polar Engineering Conference*. International Society of Offshore and Polar Engineers, 2006.

G. Oger, D. Le Touzé, D. Guibert, M. de Leffe, J. Biddiscombe, J. Soumagne, and J.G. Piccinali. On distributed memory MPI-based parallelization of SPH codes in massive HPC context. *Computer Physics Communications*, 200:1–14, 2016.

P. Reichl, K. Hourigan, and M. Thompson. The Unsteady Wake of a Circular Cylinder near a Free Surface. *Flow, Turbulence and Combustion*, 71(1-4):347–359, 2003.

P. Reichl, K. Hourigan, and M. C. Thompson. Flow past a cylinder close to a free surface. *Journal of Fluid Mechanics*, 533:269–296, 6 2005.

E. Rossi, A. Colagrossi, B. Bouscasse, and G. Graziani. The Diffused Vortex Hydrodynamics method. *Communications in Computational Physics*, 18(2): 351–379, 2015.

E. Rossi, A. Colagrossi, D. Durante, and G. Graziani. Simulating 2D viscous flow around geometries with vertices through the Diffused Vortex Hydrodynamics method. *Computer Methods in Applied Mechanics and Engineering*, 302:147–169, 2016.

J. Sheridan, J.C. Lin, and D. Rockwell. Metastable states of a cylinder wake adjacent to a free surface. *Physics of Fluids (1994-present)*, 7(9):2099–2101, 1995.

J. Sheridan, J.C. Lin, and D. Rockwell. Flow past a cylinder close to a free surface. *Journal of Fluid Mechanics*, 330:1–30, 1 1997.

P.N. Sun, A. Colagrossi, S. Marrone, and A.M. Zhang. Detection of Lagrangian Coherent Structures in the SPH framework. *Computer Methods in Applied Mechanics and Engineering*, 305:849–868, 2016.

P.N. Sun, A. Colagrossi, S. Marrone, and A.M. Zhang. The $\delta plus$-SPH model: Simple procedures for a further improvement of the SPH scheme. *Computer Methods in Applied Mechanics and Engineering*, 315:25–49, 2017.

P.N. Sun, A. Colagrossi, S. Marrone, M. Antuono, and A.M. Zhang. Multi-resolution Delta-plus-SPH with tensile instability control: Towards high Reynolds number flows. *Computer Physics Communications*, 224:63–80, 2018.

R. Vacondio, B.D. Rogers, P.K. Stansby, P. Mignosa, and J. Feldman. Variable resolution for SPH: a dynamic particle coalescing and splitting scheme. *Computer Methods in Applied Mechanics and Engineering*, 2013.

H.K. Versteeg and W. Malalasekera. *An introduction to Computational FluidDynamics,the Finite Volume Method*. Harlow: Longman Scientific and Technical, 1995.